



HAL
open science

In-field measurement and numerical modelling of air leakage in concrete: From laboratory specimen to structural full-scale

S. Multon, Donatien Rossat, Jerome Verdier, David Bouhjiti, Hognon Sogbossi, Julien Baroth, Ali Nehme, Frédéric Dufour, Hugo Gérard Jacques Cagnon, Matthieu Briffaut

► To cite this version:

S. Multon, Donatien Rossat, Jerome Verdier, David Bouhjiti, Hognon Sogbossi, et al.. In-field measurement and numerical modelling of air leakage in concrete: From laboratory specimen to structural full-scale. *Construction and Building Materials*, 2023, 385, pp.131410. 10.1016/j.conbuildmat.2023.131410 . irsn-04106727

HAL Id: irsn-04106727

<https://irsn.hal.science/irsn-04106727v1>

Submitted on 25 May 2023

HAL is a multi-disciplinary open access archive for the deposit and dissemination of scientific research documents, whether they are published or not. The documents may come from teaching and research institutions in France or abroad, or from public or private research centers.

L'archive ouverte pluridisciplinaire **HAL**, est destinée au dépôt et à la diffusion de documents scientifiques de niveau recherche, publiés ou non, émanant des établissements d'enseignement et de recherche français ou étrangers, des laboratoires publics ou privés.



Distributed under a Creative Commons Attribution - NonCommercial - NoDerivatives 4.0 International License

In-field measurement and numerical modelling of air leakage in concrete: from laboratory specimen to structural full-scale

S. Multon^{1,*}, D. Rossat², J. Verdier¹, D. Bouhjiti³, H. Sogbossi¹, J. Baroth², A. Nehme¹, F. Dufour², H. Cagnon¹, M. Briffaut²

¹ *Université de Toulouse; UPS, INSA; LMDC (Laboratoire Matériaux et Durabilité des Constructions); 135, avenue de Ranguéil; F-31 077 Toulouse Cedex 04, France*

² *Univ. Grenoble Alpes, CNRS, Grenoble INP, 3SR, F-38000 Grenoble, France*

³ *IRSN, PSN-EXP/SES/LMAPS, F-92262 Fontenay aux Roses, France*

Abstract

This work estimates air leakage through concrete porosity for structures by using data obtained in field combined with stochastic finite element (SFE) modelling. For this purpose, a methodology is proposed to evaluate permeability under representative over-pressurization conditions based on in-field measurements under vacuum. This makes it possible to investigate the air leakage through the inner wall of a 1:3 scaled nuclear vessel named the VeRCoRs mock-up. Measurements are made for over 80 points scattered on the external face of the inner wall of the structure. Based on the data collected, a statistical analysis quantifies the spatial variation of permeability and contributes to the building of an SFE model of air leakage at the structural scale. Measured and predicted data are in good agreement on the service life of the structure. This shows the relevance of combining in-field measurements during an operational phase and the SFE modelling for better evaluation of the structural performance. The lessons learnt from the present work could be useful for the assessment of all structures with durability or mechanical issues that induce a continuous loss of tightness.

Keywords

Air leakage, concrete structures, permeability measurement, stochastic analysis, VeRCoRs mock-up.

* Corresponding author, *e-mail address: Stéphane Multon, multon@insa-toulouse.fr*

26 **1 Introduction**

27 The durability of concrete is a major issue in the management of civil engineering structures
28 and induces the need for continuous monitoring of their behaviour to ensure the safety of both
29 the structure and the surrounding environment. The dimensions of large structures (which can
30 reach 1 metre in thickness and several dozens of metres in length in certain strategic structures),
31 the presence of reinforcement and, possibly, of prestressing cables, make the in-depth
32 evaluation of concrete properties over time difficult; especially when only non-destructive
33 techniques can be used.

34 Much research is currently taking place on this topic as such techniques appear promising. In
35 the case of nuclear vessels, the concrete constituting the confinement enclosures must have low
36 transport properties to guarantee the tightness of the walls and to prevent the release of
37 radioactive products into the environment throughout its lifetime. The permeability test
38 provides a reliable and fast quantification of gas transport for such applications, and regular
39 measurements must be made throughout the service life of these structures. Local permeability
40 measurements are complementary to the usual pressurization tests where the main goal is to
41 measure the global tightness to prevent any excessive leakage. However, the reliable
42 quantification of such local quantities remains a challenge because of the large external surface
43 area (need for numerous measurements), the thickness (difficulty of measuring permeability in
44 the wall core) and, predominantly, the natural variability of the properties of concrete. Hence,
45 when such large structures are assessed, the use of mean values of properties is not sufficient;
46 a stochastic approach is of great interest.

47 The present paper focuses on the evaluation of air leakage through concrete in structures
48 representative of nuclear vessels by using testing techniques coupled with stochastic Finite
49 Element (FE) modelling. From the experimental point of view, the Cembureau test is the
50 laboratory technique most commonly used on small specimens to measure their air permeability

1
2
3
4
5
6
7
8
9
10
11
12
13
14
15
16
17
18
19
20
21
22
23
24
25
26
27
28
29
30
31
32
33
34
35
36
37
38
39
40
41
42
43
44
45
46
47
48
49
50
51 under pressure [1]. It cannot be used for in-field measurement unless it is performed on cores
52 drilled from the structures, which is not possible in the case of operating nuclear vessels.
53 Different techniques (mostly vacuum techniques) currently exist for in-field measurements of
54 air permeability [2–8].

55 The first part of this paper is dedicated to the research significance to underline the scientific
56 issues concerning the measurement of air permeability in field and the stochastic evaluation of
57 the leakage rate of the VeRCoRs mock-up¹ [9,10]. In the second part, the concrete mix-designs
58 are described. In the third par, the method to evaluate the permeability under pressure based on
59 in-field measurements under vacuum is presented. The fourth part deals with an experimental
60 investigation of the mock-up using the previous technique. Measurements are made at 80 points
61 scattered on the external side of the reinforced wall of a mock-up representative of containment
62 vessels. At the structural scale, the transport properties of the wall are assumed to be the same,
63 except for the natural dispersion of the building material. Based on the data collected, statistical
64 analyses are performed to quantify the spatial variation of permeability at the structural scale.
65 The fifth and last part presents a stochastic FE model of the air leakage in VeRCoRs. The
66 numerical results in terms of global air leakage are compared with the results observed during
67 the pressurization tests.

68 **2 Research significance**

69 In the field, the main obstacles to performing relevant measurements of concrete air-
70 permeability are the difficulty of controlling the air flow in the structure (and thus the geometry
71 of the concrete volume investigated) and the type of flow regime. Due to the large size of most
72 concrete structures, e.g., the thickness of the inner wall of a nuclear containment building

59
60
61
62
63
64
65
¹ The VeRCoRs mock-up is a 1:3 scaled nuclear containment building and a research programme aiming to better understand the long-term behaviour of Nuclear Power Plants

73 (NCB), which is about 1 m, no in-field techniques can guarantee a truly steady state
74 measurement and a unidirectional flow as in laboratory conditions.

75 Technical solutions were proposed in the literature to evaluate the air permeability in field [2–
76 6,8,11]. To control the air flow, Torrent proposed a vacuum technique (*Figure 1*) based on the
77 complementarity of two cylindrical cells ([2] – *Figure 2*). During a first stage, the two cells were
78 subjected to a vacuum for 60 seconds (*Figure 2*). During the second stage, the vacuum was no
79 longer imposed. Due to the pressure difference, air flowed from the concrete towards the central
80 cell. The pressure in the cell increased and Torrent has proposed an evaluation of the
81 permeability from the pressure increase measured in the central cell during less than 15 minutes.
82 At this stage, the pressure in the external cell was equal to the pressure in the central cell thanks
83 to the use of a pressure regulator [2]. As the pressure was the same in the two cells, the air flow
84 was controlled [2].

85

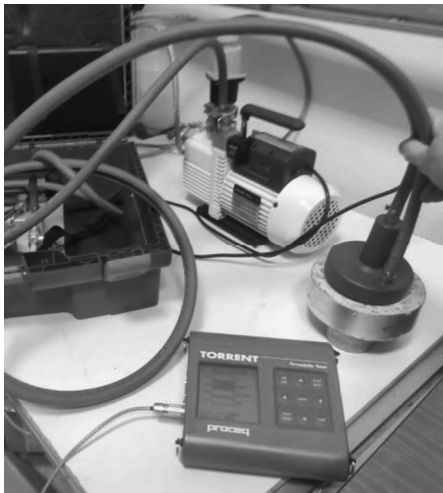


Figure 1: Torrent device for permeability measurement (acquisition system, pump and Torrent's cell on a laboratory sample)

86

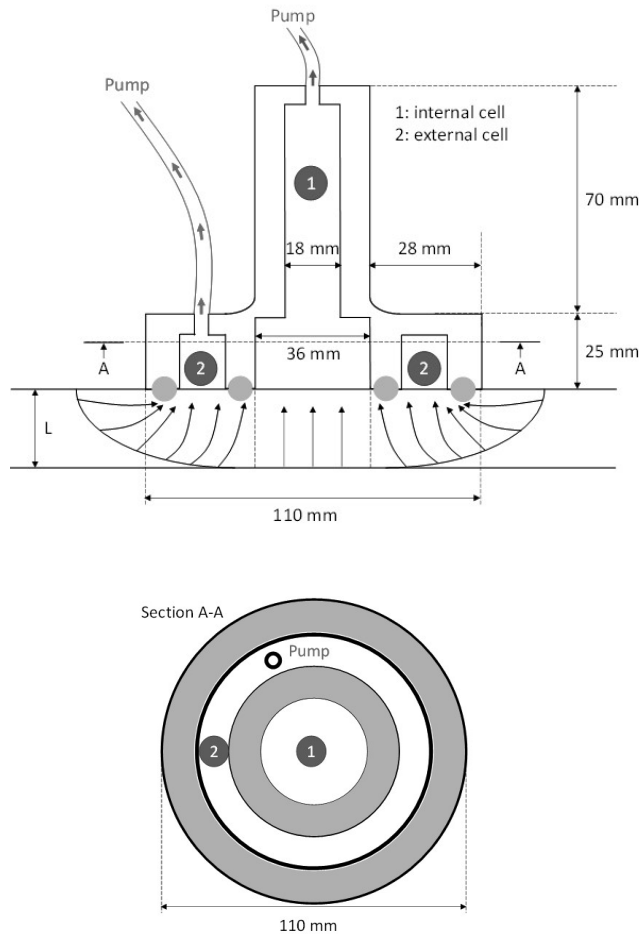


Figure 2: Pictorial representation of Torrent device for permeability measurement

87 It was first necessary to compare measurements under pressure and in vacuum. This comparison
 88 has been made on laboratory samples for steady state and unsteady state in [7,12]. The mean
 89 free paths of gas molecules are greater in vacuum than in overpressure. However, the use of
 90 Klinkenberg theory [7,12,13] made it possible to evaluate the air permeability under pressure
 91 from permeability evaluated in vacuum.

92 The objectives of the work presented here were to apply the methodology previously presented
 93 for small laboratory samples (50 mm thick) in [12], to in-field measurements made on the wall
 94 of the VeRCoRs mock-up and to provide input data to a stochastic FE model of air leakage
 95 evaluation. VeRCoRs has been specifically designed to study the safety and ageing of
 96 containment walls, with particular emphasis on predicting the leakage rate [10]. Several

1 97 numerical studies have been performed to evaluate the mechanical behaviour, with a particular
2 98 focus on cracking, and the leakage rate at different times of the mock-up [14–17]. In these
3
4 99 studies, the numerical work was mainly focused on the leakage through cracks [15]. In [17],
5
6
7 100 special attention was given to the porosity leakage (air leakage through concrete porosity). But
8
9 101 because of the lack of data, the permeability was chosen after literature review [17,18]. The
10
11 102 present study focused mainly on the porosity leakage, which is an important contributor to the
12
13 103 total leakage of the structures. The aim was, first, to use the permeability data measured in situ
14
15 104 to refine the prediction of the porosity leakage with data obtained on the concrete used in field.
16
17 105 Furthermore, the stochastic approach allows the description of the variability of the
18
19 106 permeability field of the structure in a probabilistic setting. In this context, the proposed model
20
21 107 can predict the leakage rate of the structure with the associated uncertainties, which has never
22
23 108 been done before. Several random variables, e.g. the hydric diffusivity for drying, the initial
24
25 109 water content in the concrete, the air permeability and its pressure dependence, impact the
26
27 110 modelling of the physical problem. In this study, the spatial variability of the permeability is
28
29 111 evaluated from measurements in situ whereas the variability of the other input is considered as
30
31 112 uniform in the structure. Finally, the leakage predictions based on this probabilistic approach
32
33 113 are compared with in situ measurements of the leakage rate of the structure during
34
35 114 pressurization tests.

34 115 **3 Material characterization**

36 116 The laboratory experimental work was performed with three concrete mix-designs, referenced
37
38 117 as C1, C2 and C3, representative of a wide range of usual concrete based on Portland cement
39
40 118 (**Table 1**). Three water/cement (W/C) ratios between 0.4 and 0.55 (**Table 1**) were used to obtain
41
42 119 a range of accessible porosity between 14% and 18% (**Table 2**). Water porosity was measured
43
44 120 between total saturation of the sample with water after exposure to vacuum and drying at 105
45
46
47
48
49
50
51
52
53
54
55
56
57
58
59
60
61
62
63
64
65

121 °C. The usual trend of porosity was obtained: increase in water porosity with increase in W/C
 122 ratio.

123 The study focused mainly on the characterization of the concrete C2. It was representative of
 124 the VeRCoRs mock-up and was the subject of a larger project [19]. Several batches of this
 125 concrete were produced during the course of the project. The two other concrete mixes (C1 and
 126 C3) were cast specifically for this study, and only one batch was produced. Permeability
 127 measurements were evaluated on two batches of concrete C2, referenced as C2-B1 and C2-B2.
 128 To stabilize the cement hydration, specimens were cured in lime water at a temperature of $20 \pm$
 129 2 °C for about 60 days after casting [20]. The properties of the four concrete batches of the
 130 three mix-designs after the curing period are given in **Table 2**. After 60 days in limewater, the
 131 hydration of CEM I cement is usually stabilized [20]. Therefore, the evolutions of the
 132 mechanical and air permeability after 60 days should be therefore limited [21–24].

133 **Table 1.** Concrete mixes

Constituents [kg/m ³]	C1	C2	C3
Sand 0/4	941	830	858
Gravel 4/11 R	-	445	-
Gravel 8/16 R	-	550	-
Gravel 4/12.5 R	1020	-	945
Cement CEM I 52.5 NCE CP2 NF	280	320	400
Plasticizer	2	2.4	3
Efficient water	155	167	171

135 **Table 2.** Concrete properties

	C1	C2-B1	C2-B2	C3
Water porosity (%)	18	16.7	15.2	14
Young's modulus (MPa)	31700	32300	39200	38800
Compressive strength* (MPa)	40.2	41	46.8	57.8

136 *Uniaxial compressive strength after 28 days

137 Experiments were performed on usual laboratory samples for Young's modulus and
138 compressive strength (110 mm diameter and 220 mm height) and permeability measurement (150
139 mm diameter and 50 mm thickness).

140 The objective of the experimental work was to verify the ability of the proposed approach to
141 evaluate the permeability property under pressure from the measurement under vacuum. To
142 evaluate the method, it was important to test it on materials with various porosity values. Thus,
143 the permeability was measured with the different methods on samples with saturation degrees,
144 between 3% and 70%. The accessible porosity ranged from 5 to 18%. The saturation ratio of
145 all the specimens was controlled by the following conditioning to limit thermo-hydric gradients
146 and resulting skin cracking [25–27]:

- 147 1. Saturation: Specimens were water saturated under vacuum,
- 148 2. Drying: Specimens were dried with an increasing drying temperature (40 °C to obtain a
149 saturation of 80%; 50 °C to obtain saturation levels of 60, 30 and 10%; 80 °C to obtain
150 a saturation of 3%; and 105 °C to obtain the driest state in this study, corresponding to
151 zero saturation). Targeted masses were evaluated from the porosity measured on other
152 samples cast with the same batch of concrete.
- 153 3. Homogenization: Specimens were placed in sealed conditions (aluminium and sealed
154 bags) once the target mass had been reached and put back into the oven (for a minimal
155 duration equal to the drying time in order to slightly homogenize the water distribution
156 throughout the sample).

157 The saturation levels representative of the real structure are between 30 and 80%. In the
158 laboratory, these saturation levels were all obtained with a drying temperature lower than 50 °C
159 to avoid the modification of the cement hydrates and the development of drying cracks. All the
160 calculations made for the mock-up in this paper were based on these representative values.
161 Drying at 80 °C and 150 °C was performed only to have common reference values for porosity

162 and permeability measurements. The smallest saturation ratio obtained after a 105 °C drying
163 process was taken to be 0% of saturation in this work.

164 **4 Experimental methodology**

165 The objective of this section is to propose an evaluation of intrinsic permeability (permeability
166 corresponding to viscous flow and assumed to be independent of fluid and test conditions) and
167 to quantify the dependence of air permeability to pressure from permeability measurement in
168 vacuum. The technique of in-field measurement of permeability was first evaluated in the
169 laboratory and compared to the standardized technique for permeability measurement.

170 **4.1 Experimental techniques for in-field permeability measurement**

171 *4.1.1 Evaluation of the air permeability by means of an increase of pressure after* 172 *vacuum*

173 In their experimental works of 1995, Yssorches et al. [28] used a permeability measurement
174 based on a vacuum technique. During the measurement, a vacuum was imposed on one face of
175 a concrete sample for a certain time (0 or 2 hours), then the permeability was evaluated from
176 the pressure increase when the pumping was stopped [28]. This technique was used for samples
177 with small thickness and the direction of the air flow was controlled by an external seal. The
178 permeability evaluated in the first stage of the pressure increase was not representative of the
179 real permeability [28]. The authors showed that, for small samples in the laboratory, the
180 increase became almost linear after a long period of time (at least 15 minutes). They recommend
181 that permeability should be evaluated from the slope of the increase when the regime is
182 stabilized. For small samples, stabilization is obtained when the air flow crosses the thickness
183 completely. As the pressure was not maintained constant, the flow was never perfectly constant:
184 the pressure profile in the thickness of the sample was never perfectly stabilized (but the
185 variation with time became small) and the regime was pseudo-steady [28].

186 At the beginning of the pressure increase, the regime seems to be disturbed by the modification
 187 of the boundary conditions, particularly for a small duration of vacuum [28]. The sudden
 188 stopping of the pumping and the moisture gradient in the concrete skin may be responsible for
 189 this effect. As the first centimetres of concrete are usually dryer than in depth, the depth
 190 investigated increases fast at the beginning of the pressure increase (occurring in dry concrete)
 191 and slows down when the air flow reaches deeper concrete with a higher saturation ratio.
 192 Therefore, the interpretation of the pressure increase in the central cell of Torrent's apparatus
 193 has been analysed based on the conclusions obtained in [28]. Once the pseudo-steady regime is
 194 obtained in the central cell, the apparent permeability (in fine concrete porosity, air flow
 195 depends on pressure because of the slip effect on pore wall due to molecular contribution –
 196 apparent permeability is thus equal to the sum of viscous and slip flows [29]) and can be
 197 deduced from the Hagen-Poiseuille equation and from the conservation of the air mass between
 198 the concrete porosity and the volume of the cell [13,30]:

$$k_{a_{psr}} = \frac{2 \cdot \mu \cdot L}{A \cdot (P_{atm}^2 - P_c^2)} \cdot V_c \cdot \dot{P}_c \quad Eq. 1$$

199 with $k_{a_{psr}}$ the apparent permeability obtained during the pseudo-steady regime, μ the air
 200 viscosity, L and A the thickness and the cross-section of the sample, respectively, P_{atm} the
 201 atmospheric pressure, V_c the volume of the cell, P_c the pressure in the cell and \dot{P}_c the initial slope
 202 of the pressure increase in the cell.

203 In the work presented here, the saturation ratio, the accessible porosity and the apparent
 204 permeability are considered constant and homogenous in the depth investigated, as is usual for
 205 such measurements.

206 Due to the large thickness of the walls of real structures, and particularly for vessels of nuclear
 207 plants, the vacuum time needed is too long for permeability measurement to be performed in
 208 such controlled conditions. The main difficulty is then to evaluate the depth of concrete

209 impacted by the air flow. In his approach, Torrent proposed an evaluation of this depth, L_0 ,
 210 from the mass balance of air moles crossing the concrete to reach the central cell during the test
 211 [2]:

$$L_0 = \sqrt{\frac{2 \cdot k_{a_t} \cdot P_{atm} \cdot (t_v + t)}{\varphi \cdot \mu}} \quad Eq. 2$$

212 with: k_{a_t} the unknown permeability of concrete crossed by the air flow, t_v the vacuum time, t
 213 the time after the pumping was stopped, φ the porosity of concrete, and μ the air viscosity.

214 The combination of the two previous equations enables the permeability, k_{a_t} , to be evaluated
 215 from the evolution of the pressure in the central cell for any time, t , by the following equation:

$$k_{a_t} = \frac{8 \cdot \mu}{\varphi} \cdot \left(\frac{V_c}{A}\right)^2 \cdot \frac{P_{atm}}{(P_{atm}^2 - P_c^2)^2} \cdot \dot{P}_c^2 \cdot (t_v + t) \quad Eq. 3$$

216 The air flow rapidly becomes almost constant across the concrete (pseudo-steady state) for
 217 specimens with small thickness and large permeability. The permeability can thus be evaluated.

218 For intermediate permeability, the air flow can cross the thickness (only the external surface is
 219 at atmospheric pressure), but the duration of the pressure increase is too small for the pseudo-
 220 steady state to be reached. For such short times, the permeability should be evaluated by Eq. 1.
 221 but an overestimation of the permeability is probable [28]. For specimens with same thickness
 222 and lower permeability, the air flow does not cross the thickness (part of the concrete inside the
 223 sample is still at atmospheric pressure). Eq. 3 should be used to calculate the permeability.

224 With Eq. 3, the evaluation of the permeability is based on the evaluation of the depth, L_0 , (Eq.
 225 2) of the concrete investigated. The evaluation of L_0 depends on the concrete accessible porosity
 226 [2]. The accessible porosity for air molecules in the field depends on the concrete saturation
 227 ratio and the accuracy of the permeability measurement depends on the accuracy of the concrete
 228 porosity estimation. Various non-destructive methods have been proposed to evaluate the

229 concrete saturation ratio [31–34]. For the evaluation of L_0 , the linearity of pressure is assumed
1
2 230 through a certain depth of concrete [2]. The profile is not really linear along this depth and this
3
4 231 can lead to an incorrect estimation of the permeability. To improve the technique, it is important
5
6
7 232 to evaluate the time for which the evaluation of L_0 is the most relevant, for small, average or
8
9 233 long durations of pressure increase.

12 4.1.2 Application

13 234 This determination of the permeability measured under vacuum was applied to three samples
14
15 235 of the three mix-designs presented above (Tables 1-2) for different saturation ratios (Figure 3).
16
17 236

18
19 237 The pressure increase with time of the sample C2 (batch B2), obtained with Torrent’s apparatus
20
21
22 238 ([2] – Figure 1), is shown in Figure 3 for three saturation ratios (65, 33 and 10%).
23

24
25 239 The apparatus is automated to stop the pressure increase after a variation of about 20 mbars, or
26
27 240 after 660 seconds (Figure 3). The slope was evaluated for the last two minutes of the increase.
28

29
30 241 From the slope given by the pressure increase recorded by Torrent’s apparatus, it is possible to
31
32 242 evaluate the concrete permeability in vacuum conditions: using Eq. 1 if the sample is crossed
33

34 243 by the air flow, or by using Eq. 3 if the air flow does not reach the other side of the sample.
35
36

37 244 This is determined from Eq. 2. If L_0 is less than 50 mm, then k_{at} is the permeability under
38
39 245 vacuum. If L_0 is more than 50 mm, then k_{apvr} is the permeability under vacuum. For the three
40

41
42 246 concrete mix-designs, most of the samples with saturation ratios lower than or equal to 30%
43
44
45 247 were crossed by the air flow. Most of the other samples were not crossed.
46
47
48
49
50
51
52
53
54
55
56
57
58
59
60
61
62
63
64
65

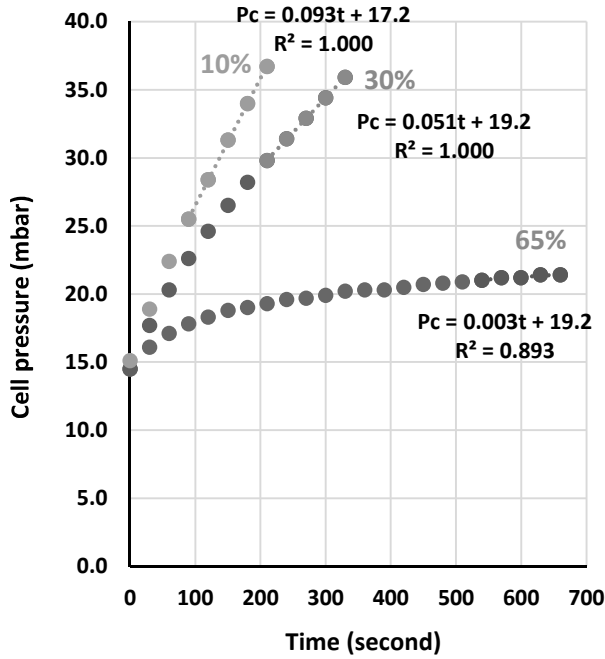


Figure 3: Increase of pressure in the central cell of the apparatus and determination of the slope for evaluation of the permeability of a given sample at 3 different saturation ratios (10, 30 and 65%)

The apparent permeability obtained for the three concrete mix-designs at the different saturation ratios is shown in Figure 4. As expected, the permeability changes significantly for small variations of saturation ratios above 60% [35].

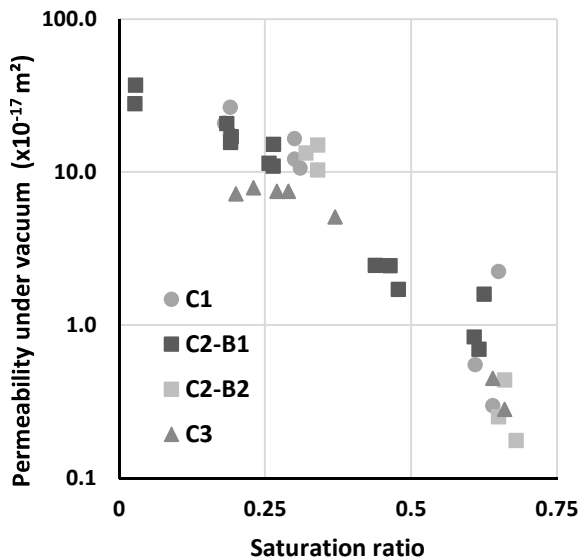


Figure 4 : Apparent permeability obtained under vacuum according to the saturation ratio (logarithmic vertical axis)

4.2 Comparison with Cembureau technique

4.2.1 Cembureau permeability as a reference for the permeability measurement

The objective of this work was to evaluate the intrinsic permeability, denoted k_i , and usually evaluated under pressure, from the permeability under vacuum. For this purpose, the concrete permeability evaluated with the Cembureau technique was defined as the reference permeability ([1] – Figure 5). Permeability measurement with the Cembureau technique is based on the steady state measurement of a unidirectional air flow crossing the cross-section of a sample subjected to a constant pressure gradient lying usually between 1 and 4 bar.

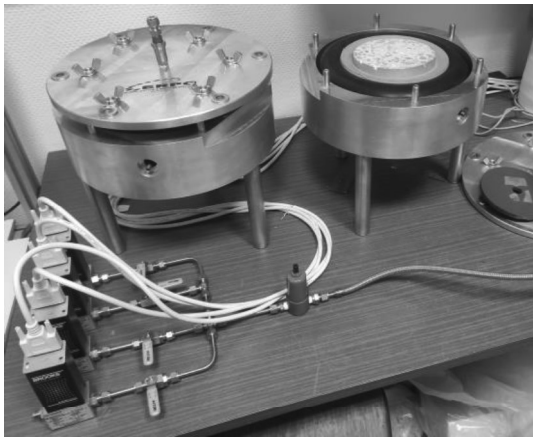


Figure 5: Cembureau device for permeability measurement in laboratory

For each sample, the apparent permeability under pressure was evaluated at 4 pressure levels by applying 2, 3, 4 and 5 (or 6) bars to one face of the sample while the other face was under atmospheric pressure. The relationship between the apparent permeability and the reciprocal of the mean pressure of the test is linear. This relationship is commonly referred to as Klinkenberg's law. Intrinsic permeability (ordinate to the origin of this line) and the slope were evaluated for every sample and every saturation ratio. The values for a sample of concrete C2-B1 at 4 saturation ratios are shown in Figure 6.

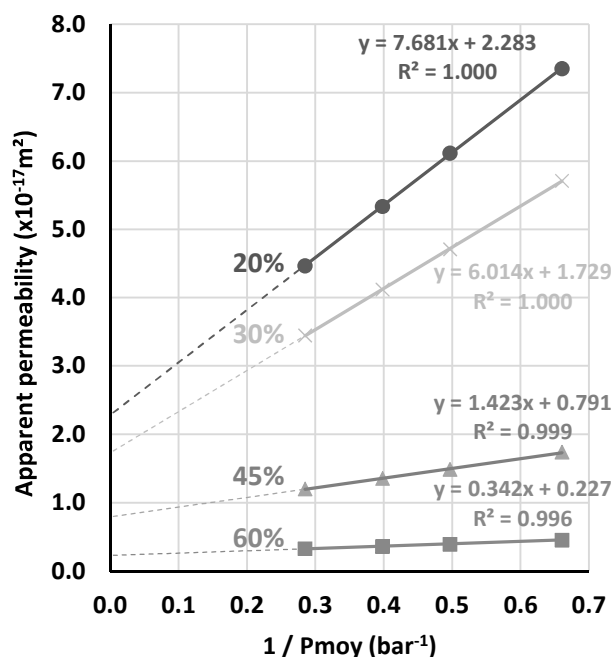
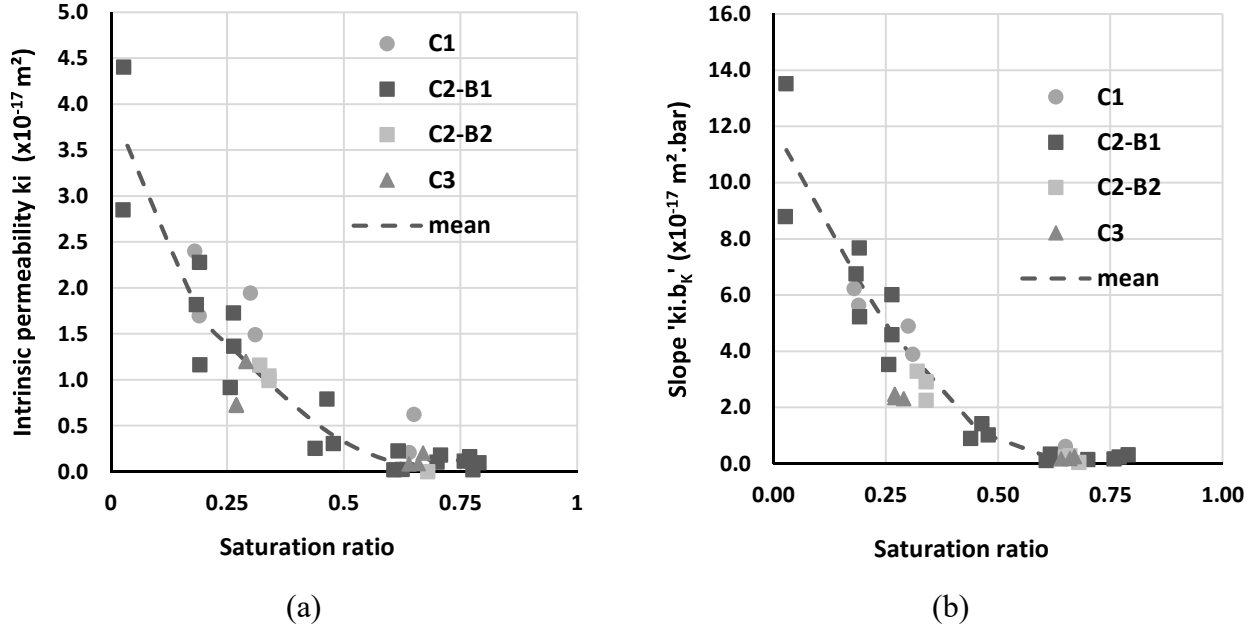


Figure 6: Apparent permeability versus the inverse of the mean pressure for Cembureau tests performed on a single sample at 4 different saturation ratios (20, 30, 45 and 60%)

These tests were performed on all the samples of the experimental programme with a focus on usual in situ saturation ratios in concrete, i.e. between 20 and 80%. Above 70-80% of saturation, the three concretes were air-tight (see Figure 7). At 60%, the concrete C1 showed the greatest permeability. At 30%, the differences in permeability were small and close to the usual scatter found on permeability measurements. However, the permeability trend for the three mixes was similar to the water porosity trend: permeability increased with increasing W/C ratio (Figure 6). Under 20% saturation, concrete samples were exposed to 80 °C. This led to significant thermo-hydric damage [36]. It increased permeability discrepancy (Figure 7) and the concrete was no longer representative of usual exposure conditions of structures. It was only performed for one concrete in this study (Figure 7).



285 Figure 7: Reference intrinsic permeability (a) and reference slope of Klinkenberg's law (b) versus saturation ratio
 286 for the three concretes

287 4.2.2 Determination of the intrinsic permeability from a single permeability measurement

288 To be able to evaluate the air leakage of a structure under pressure, it is necessary to determine
 289 both the intrinsic permeability and the slope of Klinkenberg's law [29]:

$$k_a = k_i \left(1 + \frac{b_k}{P_m} \right) \quad \text{Eq. 4}$$

290 with k_a the apparent permeability, k_i the intrinsic permeability, P_m the mean pressure between
 291 the atmospheric pressure and the pressure of the test, and b_k , the Klinkenberg gas slippage
 292 factor.

293 Apparent permeability measured in vacuum for different pressures is close to the prolongation
 294 of Klinkenberg's law for the domain of pressure lower than atmospheric pressure [12,13].

295 However, the slope of the variation of the apparent permeability with pressure for
 296 measurements in vacuum does not correspond to the slope of Klinkenberg's law [12]. It is thus
 297 not possible to evaluate the slope by measuring permeability with different input pressures in
 298 vacuum. Sogbossi et al. [12] proposed an evaluation of the intrinsic permeability from a single
 299 permeability measurement (under pressure or in vacuum) based on theoretical and empirical

300 concepts [13,29,37]. From Klinkenberg's theory [29], the following relationship has been
 1
 2 301 established:

$$k_{a_2} = C_P k_{a_P} \quad \text{Eq. 5}$$

302 with k_{a_2} the apparent permeability for an absolute pressure of 2 bars, and k_{a_P} the apparent
 9
 10 303 pressure for any pressure P . C_P is a function of the pressure and of the pore network. Many
 11
 12 304 authors have shown the relation between the apparent permeability and the characteristic
 13
 14 305 dimensions of the pore network of porous media [13,38–45]. Permeability could thus be
 15
 16 306 evaluated from the pore size distribution obtained by Mercury Intrusion Porosimetry [43].
 17
 18 307 Sogbossi's PhD thesis [13] proposed the evaluation of C_P , linking the apparent permeability at
 19
 20 308 different pressures, as a mean value calculated for the smallest pores of the network lying
 21
 22 309 between a minimal value R_0 and a maximal value R_1 [12,37]:

$$\overline{C_P} = \overline{C_P} = \frac{1}{R_1 - R_0} \int_{R_0}^{R_1} \left(\frac{r + 0.171}{r + 0.268/P_m} \right) dr \quad \text{Eq. 6}$$

310 with P_m the real mean pressure between the atmospheric pressure and the pressure of the test,
 34
 35 311 P , taking the compressibility of air into account [12]. In Sogbossi's work, the values of radii
 36
 37 312 were calibrated to obtain a correct evaluation of apparent permeability in vacuum from a
 38
 39 313 measurement under pressure in the steady state.

40
 41
 42
 43 314 The result of this integral is:

$$\overline{C_P} = 1 + \frac{0.171 - \frac{0.268}{P_m}}{R_1 - R_0} \ln \left(\frac{R_1 + 0.268/P_m}{R_0 + 0.268/P_m} \right) \quad \text{Eq. 7}$$

44
 45
 46
 47
 48
 49
 50
 51 315 Thus, the intrinsic permeability and the slope of Klinkenberg's law can be evaluated from only
 52
 53 316 one permeability measurement under pressure or in vacuum.

54
 55
 56
 57 317 In the present work, this approach is first validated for the three concretes of the study under
 58
 59 318 pressure. Combining Eq. 4 and Eq. 5, the slope can be estimated with the Cembureau technique

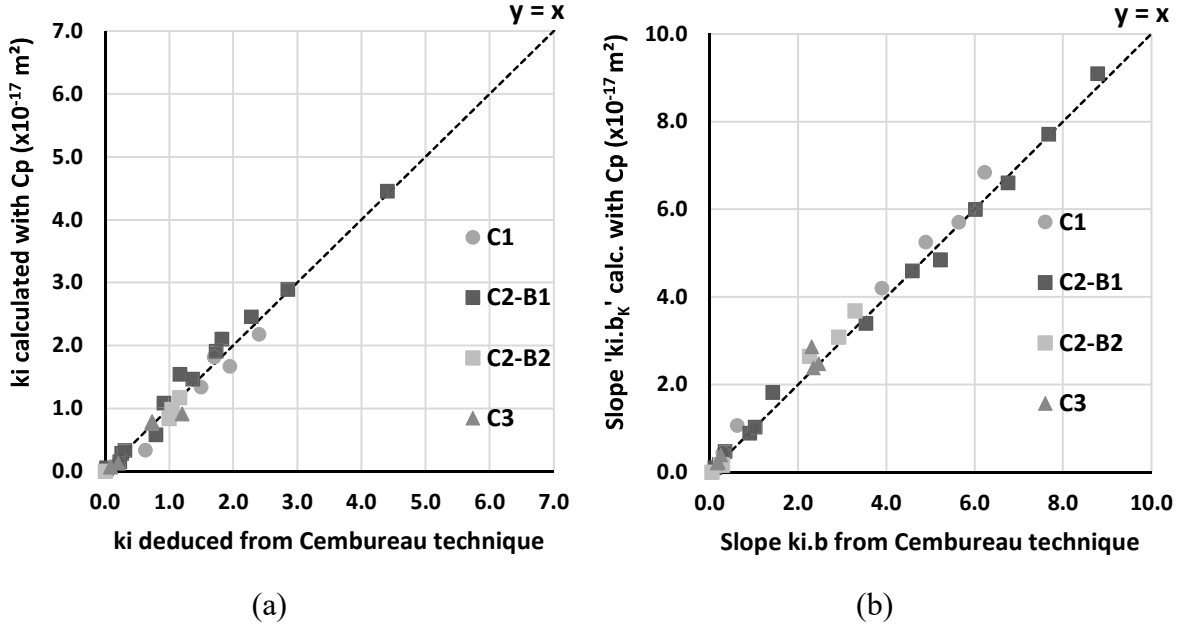
319 from the apparent permeability measured for an absolute pressure of 2 bars:

$$b_k k_i = k_{a_2} \frac{1 - \frac{1}{\overline{C_5}}}{\frac{1}{P_{m2}} - \frac{1}{P_{m5}}} \quad \text{Eq. 8}$$

320 where P_{m2} is the real mean pressure between the atmospheric pressure and 2 bars, and P_{m5} the
321 mean pressure between the atmospheric pressure and 5 bars. The intrinsic permeability can then
322 be calculated as:

$$k_i = k_{a_2} - \frac{b_k k_i}{P_{m2}} \quad \text{Eq. 9}$$

323 The two equations are valid for absolute pressures lower than 0.5 bar and higher than 2 bars. In
324 Figure 8, the results obtained with these equations are compared to the reference slope and to
325 the intrinsic permeability experimentally determined in the previous part. In the present work,
326 the maximal pore radius, R_1 , was calibrated to obtain good correspondence for the three
327 concretes and for saturation ratios between 20 and 70%, with a maximal pore radius, R_1 , of
328 0.2 μm (the minimal value, R_0 , was taken to be equal to 0.01 μm as proposed in Sogbossi's
329 work [12]). For such radii, the quantity $\overline{C_5}$ is equal to 1.58, which is consistent with the results
330 obtained during the development of the methodology [13]. The order of magnitude of this
331 maximal pore radius is consistent with radius size considered in previous numerical studies on
332 air permeability in concrete [43–45].



333 Figure 8: Comparison between the intrinsic permeability (a) and the slope of Klinkenberg's law (b) obtained by
 334 Cembureau technique and the values deduced from the apparent permeability at 2 bars and C_5 equal to 1.58
 335 (maximal radius of $0.2 \mu\text{m}$)

4.2.3 Comparison between the intrinsic permeability evaluated in vacuum and the intrinsic permeability evaluated under pressure

338 As explained above, vacuum techniques are very interesting to evaluate the permeability of real
 339 structures. As the intrinsic permeability and the slope of Klinkenberg's law cannot be evaluated
 340 directly from different apparent permeability values obtained in vacuum [12], the methodology
 341 presented just above was used. In this case, only an apparent permeability in vacuum, k_{a_v} , is
 342 known. The slope and the intrinsic permeability were obtained by combining Eq. 5, Eq. 8 and
 343 Eq. 9:

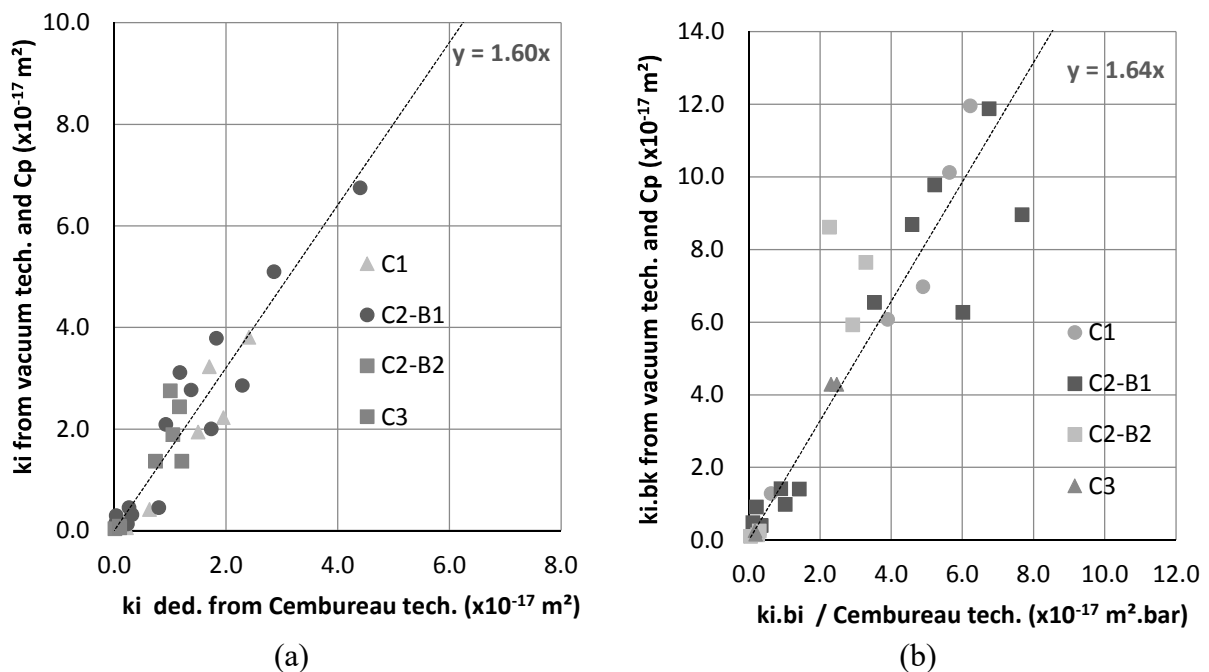
$$b_k k_i = C_v k_{a_v} \frac{1 - \frac{1}{C_5}}{\frac{1}{P_{m2}} - \frac{1}{P_{m5}}} \quad \text{Eq. 10}$$

344 and

$$k_i = C_v k_{a_v} - \frac{b_k k_i}{P_{m2}} \quad \text{Eq. 11}$$

345 C_v was determined from Eq. 7 with the same maximal radius of $0.2 \mu\text{m}$ evaluated in the previous
 346 part and from the pressure measured by the central cell of the vacuum apparatus. In this
 347 situation, C_v was about 0.545, in agreement with the previous work [13].

348 In Figure 6, the intrinsic permeability and the slope evaluated from the apparent permeability
 349 measured under vacuum (presented in Figure 4) are compared to the reference values for the
 350 intrinsic permeability and the slope determined with the Cembureau technique. This method
 351 led to an overestimation of both the intrinsic permeability and the slope, by about 60%. This
 352 result can be partly explained by the presence of parasitic fluxes on the thin samples tested, due
 353 to the geometry of the system. It is important to note that this overestimation was quite similar
 354 for the three Portland concretes used in this experimental study and could thus be extrapolated
 355 to the in-field concrete investigated in the following part.



356 *Figure 9: Comparison between the intrinsic permeability (a) and the slope of Klinkenberg's law (b), obtained by*
 357 *the Cembureau technique, and the values deduced from the vacuum permeability and C_p , for C_p equal to 0.545*

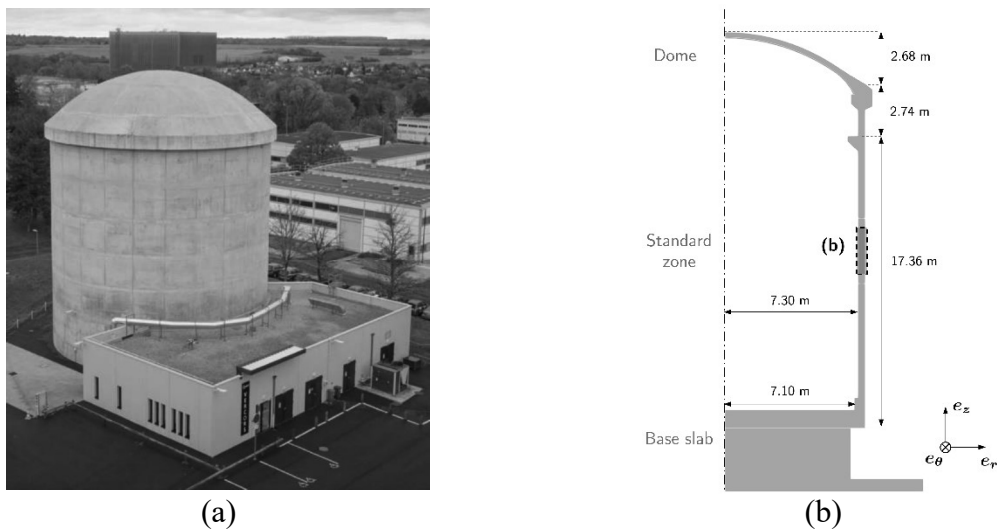
358 The experiments presented here showed that it is possible to estimate the intrinsic permeability
 359 and the slope of the Klinkenberg's law which can be used to calculate air transport under

360 pressure from a technique of permeability measurement under vacuum, with an overestimation
361 of about 60%.

363 5 In-field permeability measurement on the inner wall of an NCB mock-up

364 This section presents the location, the values and the analysis of the permeability in-field
365 measurements conducted on the VeRCoRS mock-up (Figure 7). As shown in the literature,
366 there was a lack of permeability data to precisely analyse the porosity leakage of the mock-up
367 [17] and more generally of NCB. The aim of these measurements was to build up an
368 experimental database to quantify the mean and the scatter of the air permeability of the
369 concrete constituting the mock-up.

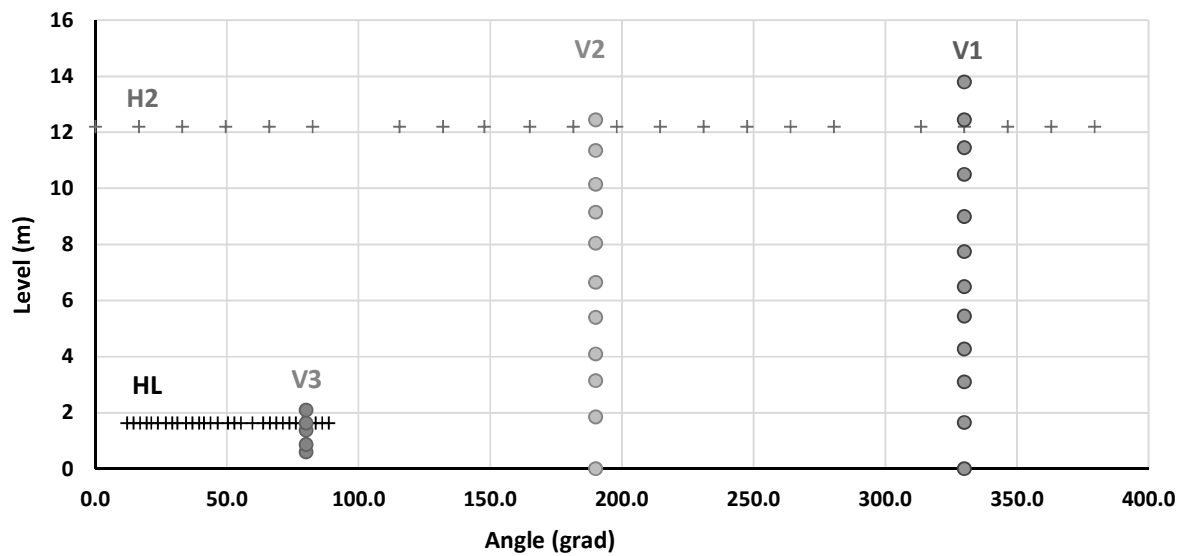
370 5.1 VeRCoRS mock-up description and locations of measurements



372 *Figure 10: Experimental 1:3 scaled double-walled nuclear containment building (NCB) – VeRCoRS mock-up:*
373 *overview – photo by EDF (a) and 2D-AXIS view of the VeRCoRS mock-up's inner wall [46] (b)*

374 A network of 80 points (Figure 11) was chosen on this 40 cm thick wall, along two horizontal
375 lines (30 points named HL along one fifth of the circumference of the mock-up in the lower
376 part at level 1.63 m, and 22 points named H2 along the whole circumference in the upper part
377 part at level 12.2 m) and along three vertical lines (5 points named V3 along the lower 2 meters for
378 the angle of 80 grad, 13 points named V2 along the whole height at 190 grad and 11 points

380 named V3 along the whole height at 330 grad). The location of the points for the permeability
 381 measurements was chosen to be representative of the concrete wall (usually far from any
 382 singularity, e.g., prestressing anchorages, gusset) and distributed on the structure (Figure 11),
 383 especially for H2, V1 and V2, to evaluate the variability of concrete on the whole structure. The
 384 distances between successive points were shortened for the lines HL (in the same batch) and
 385 V3 (different batches) to assess the dispersion of measurements in a restricted area of the
 386 structure.

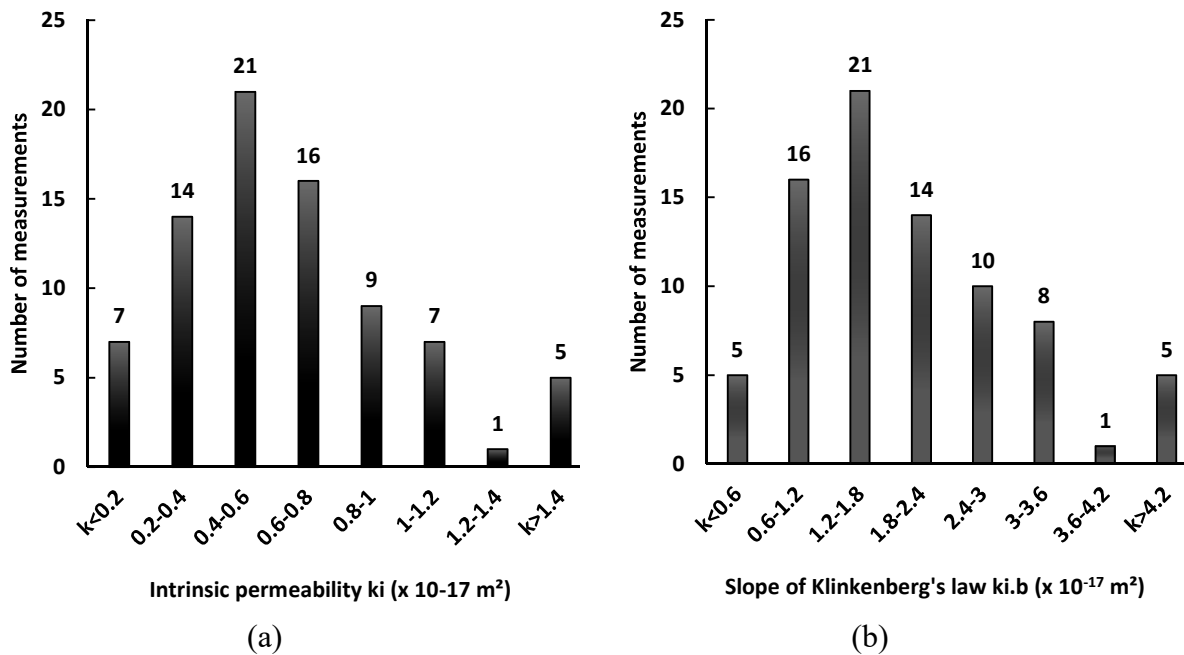


387
388 *Figure 11: Locations of the 80 points for local measurements of permeability.*

389 5.2 Measurements along horizontal and vertical lines

390 The distributions of both the intrinsic permeability and the slope for Klinkenberg's law obtained
 391 from the 80 measurements performed on the mock-up are presented in Figure 12. This
 392 evaluation was performed from an apparent permeability obtained in vacuum and from Eq. 10
 393 and Eq. 11. Means and standard deviations are given in **Table 3**. Since the two parameters were
 394 evaluated from the same measurements, their distributions were similar (Figure 12). It is
 395 important to note that a measurement is very localized, with a surface of 40 mm in diameter
 396 (Torrent apparatus). Even with 80 points, the surface area investigated was very small compared
 397 to the total surface area of the mock-up. Moreover, the measurement was superficial: the air

398 flow reached an average depth of 70 mm (Eq. 2) for a wall of 400 mm of total depth, which
 399 finally represents only 17.5% of the thickness investigated. In the field, the air permeability is
 400 not homogeneous in the thickness investigated by the technique due to the moisture gradient
 401 usual in the skin of concrete structures. Moreover, the skin of a concrete structure presents a
 402 greater proportion of mortar than the core concrete does. However, the proportion of the skin
 403 that is more permeable than the core does not impact the pressure increase during in-field
 404 measurements as the pressure increase is mainly driven by the less permeable zone of the
 405 investigated depth.



407 *Figure 12: Distributions of the intrinsic permeability (a) and of the slope of Klinkenberg's law (b) for 80*
 408 *measurements performed on VeRCoRs mock-up*

Table 3. Intrinsic permeability and slope of Klinkenberg's law for the whole distribution (in brackets the value when five points with very high intrinsic permeability are excluded)

	k_i ($\times 10^{-17}$ m ²)	$k_i \cdot b_K$ ($\times 10^{-17}$ m ²)
Number of measurements	80 (75)	80 (75)
Mean	0.677 (0.58)	2.075 (1.77)
Standard deviation	0.51 (0.29)	1.562 (0.89)

The mean intrinsic permeability in field is about 0.68×10^{-17} m² with a coefficient of variation greater than 75%. The mode is lower than the mathematical mean, the distribution is not symmetric and seems to be lognormal. The distribution was significantly influenced by the presence of five points with very large permeability (above 1.4×10^{-17} m²), which may correspond to points with important defects. These five measurements represent isolated values lying between 4.3 and 9.6×10^{-17} m², which are grouped in the last interval for the sake of simplification. Without these five points, the mean value was only about 0.58×10^{-17} m² with a coefficient of variation of about 50%. Such permeability can be obtained for saturation ratios between 35 and 50% (Figure 7). This value is in agreement with the water content measured in field [34].

The variations of permeability along both the horizontal and the vertical directions are presented in Figure 10 and **Table 4**. The horizontal line HL shows considerable scatter in permeability, particularly close to the angle of 80 grad (Figure 10) with 3 outliers. This area with high permeability corresponds to the 2 high values of permeability encountered for V3 (angle of 80 grad and height of about 1.6 m). The measurements along the other horizontal line (H2) present a scatter representative of the concrete heterogeneity. The permeability does not seem to be significantly dependent on the level of concrete (Figure 10-b). Except for 5 outliers, the permeability is quite homogeneous in the whole structure (**Table 4**) despite the use of several batches to cast the full height.

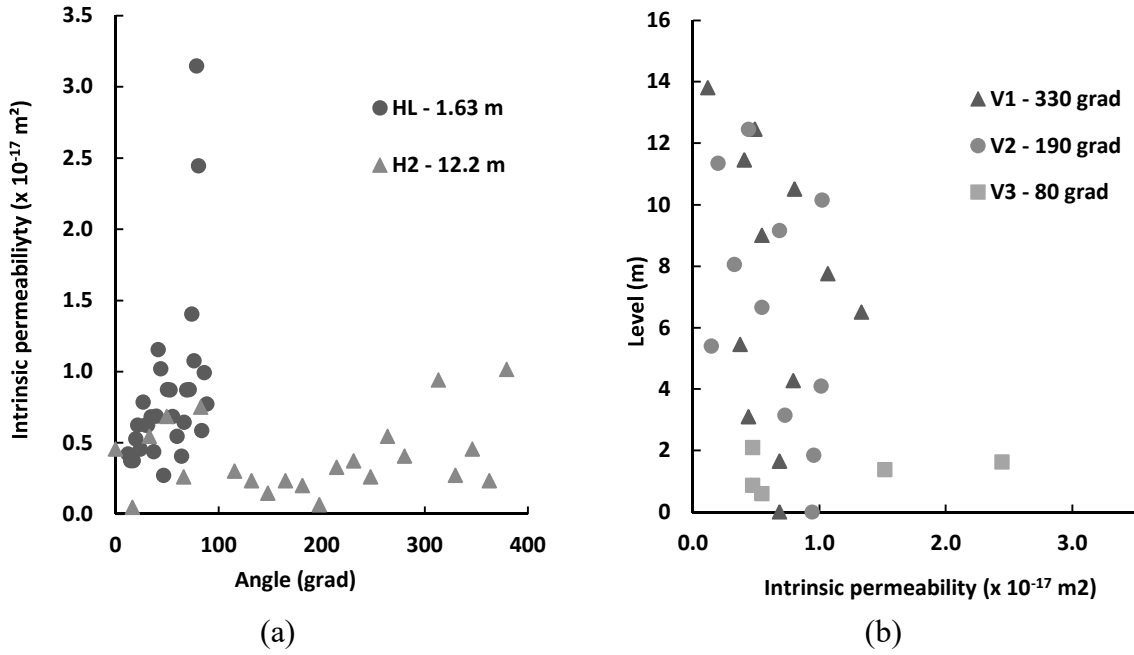


Figure 13: Intrinsic permeability along two horizontal lines (a) and three vertical lines (b) of VeRCoRs mock-up

Table 4. Intrinsic permeability by measurement lines (in brackets, excluding five points with very high permeability)

Lines	HL	H2	V1	V2	V3
Number	30 (27)	22	12	11	5 (3)
Mean	0.84 (0.68)	0.40	0.64	0.64	1.09 (0.50)
Standard deviation	0.60 (0.23)	0.26	0.33	0.33	0.88 (0.08)

With the measurements performed in field, it was possible to evaluate the distribution of the intrinsic permeability along the horizontal and the vertical directions of the mock-up. It is an essential input data of the modelling presented in the following part to evaluate the porosity leakage of the mock-up, and for all future numerical modelling of the structures which can be based on the previous works presented in [14–16].

6. Air leakage calculations using Stochastic Finite Element Methods

The objective of this section is to evaluate the spatial variability of the intrinsic permeability k_{i0} of the concrete of the VeRCoRs mock-up, and its effect on the leakage rate of the structure. The spatial variability is necessary to propose a stochastic evaluation of the air leakage of the mock-up and finally to be able to estimate a potential leakage whatever the location of the considered structure. In this perspective, random fields are used for modelling the permeability, and their

447 underlying correlation structure is identified from the non-destructive permeability
448 measurements presented in Section 5.

449 The permeability measured in field on the concrete skin was only representative of the
450 permeability in the first few centimetres of concrete, and thus, at a certain saturation degree
451 (about 40%). To obtain the global evaluation of the leakage, the saturation evolution with depth
452 had first to be evaluated by modelling. In the calculations presented below, the permeability
453 along the first few centimetres was taken equal to the in-field measurement. The evolution of
454 the permeability with depth was then calculated by the modelling from the laboratory results
455 for the evolution of permeability with saturation as explained in part 6.2 The stochastic FE
456 leakage model adopted in this study is subsequently presented, before probabilistic predictions
457 of the leakage rate of the VeRCoRs mock-up are performed.

6.1 Construction of permeability random fields

458 Let $(\Omega, \mathcal{F}, \mathbb{P})$ be a probability space, and $\mathcal{D} \subset \mathbb{R}^3$ be the spatial domain studied. The concrete
459 intrinsic permeability k_{i0} is represented by a random field that corresponds to a family
460 $K_{i0}(x, \omega)_{x \in \mathcal{D}}$ of real-valued random variables defined on the underlying probability space
461 $(\Omega, \mathcal{F}, \mathbb{P})$, which is indexed by points of the domain \mathcal{D} . Then, the intrinsic permeability field
462 may be seen as a function $K_{i0}(x, \omega)_{x \in \mathcal{D}}$ of two variables, namely a spatial coordinate $x \in \mathcal{D}$
463 and a generic outcome $\omega \in \Omega$ of the underlying probability space. The permeability field K_{i0} is
464 assumed to be a lognormal random field [46,47] and, for the sake of simplicity, the field $\log K_{i0}$
465 is assumed to be stationary, i.e. its mean function $\mu_{\log K_{i0}}$ is assumed to be constant, and its
466 covariance kernel depends only on relative spatial coordinates, which can be written:

$$C_{\log K_i}(x, x') = C_{\log K_{i0}}(x - x') = \sigma_{\log K_{i0}}^2 R_{\log K_{i0}}(x - x') \quad \text{Eq. 12}$$

469 where $\sigma_{\log K_{i0}}^2$ is the variance and $R_{\log K_{i0}}$ the correlation kernel of the field $\log K_{i0}$. Thus, the
 1
 2
 3 470 log-permeability random field $K_i \log K_i$ is fully characterized by its moments
 4
 5 471 $(\mu_{\log K_{i0}}, \sigma_{\log K_{i0}}^2)$, and its correlation kernel $R_{\log K_{i0}}(x - x')$.
 6
 7

8
 9 472 The correlation structure of the log-permeability field is identified from non-destructive
 10
 11 473 permeability measurements. Only the HL measurement set (see Section 5.2) is used with
 12
 13
 14 474 sufficiently fine spacing (approx. 0.3 m between two points). Assuming that the volume
 15
 16 475 concerned by measurements has a water saturation ratio of 50%, a mean of about $\mu_{K_0} = 7.10^{-17}$
 17
 18
 19 476 m² and a CoV of 75% are estimated from measurements presented in Section 5.2. The
 20
 21 477 associated experimental unidimensional (semi) variogram [48] is given by:

$$478 \quad \gamma_{HL}(h) = \sigma_{\log K_{i0}}^2 - C_{\log K_{i0}}(h\nu_{HL}) \quad \text{Eq. 13}$$

24
 25
 26
 27
 28 479 where $h > 0$ and ν_{HL} is the direction of the HL line. This experimental variogram is
 29
 30 480 subsequently fitted by several classical variogram models (linear, exponential and Gaussian
 31
 32
 33 481 models [48] in Figure 14). The results obtained suggest that the Gaussian model provides the
 34
 35 482 best fit, with an autocorrelation length ℓ_{ac} in the direction of the HL line. For the sake of
 36
 37
 38 483 simplicity, the log-permeability random field $\log k_0(x, \omega)$ is assumed to be isotropic, since
 39
 40 484 measurements in the vertical and radial directions are not available for constructing variograms
 41
 42
 43 485 in the three main directions. Eventually, the following correlation kernel $R_{\log K_{i0}}(x - x')$ is
 44
 45 486 considered for the log-permeability field:

$$487 \quad R_{\log K_{i0}}(x - x') = R_{HL}(\|x - x'\|) = \exp\left(\frac{-1}{2} \frac{\|x - x'\|^2}{\ell_{ac}^2}\right) \quad \text{Eq. 14}$$

488 where $\|\cdot\|$ is the Euclidean norm of \mathbb{R}^3 .

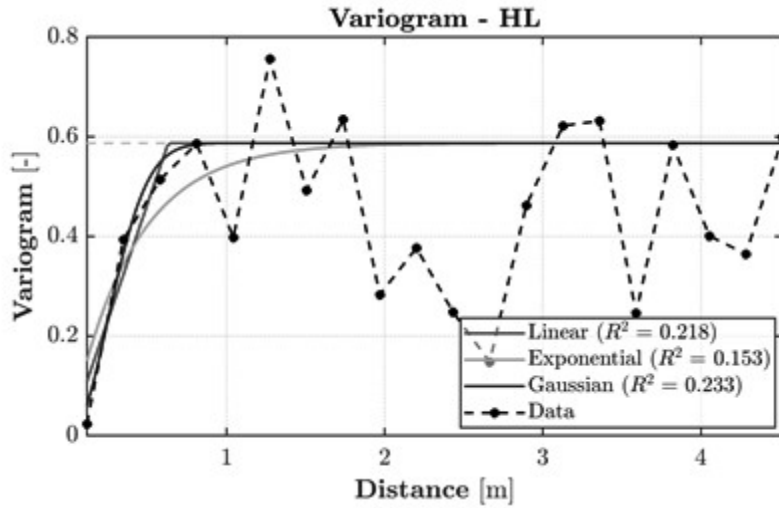


Figure 14: Experimental variogram fitting using HL measurement data.

Then, the (continuous) random field $K_{i0}(x, w)$ is approximated by a finite set of random variables $(\zeta_j)_{1 \leq j \leq r}$. In this study, we focus on three main Representative Structural Volumes (RSV) [46] of the VeRCoRs mock-up; namely its standard zone (or wall), its gusset, and its dome, all depicted in Figure 15. Three finite element meshes corresponding to these RSV are considered (see Figure 15-a-c) with a characteristic mesh size of about $l_{FE} = 0.15$ m, following recommendations of [49] concerning the discretization of random fields on an FE mesh ($l_{FE} \leq l_{ac}/3$). Moreover, each mesh corresponds to an angular sector of 15° , in order to provide dimensions larger than the fluctuation length (given by $\ell_{flu} = \sqrt{\pi} \ell_{ac} = 0.89$ m in the case of a Gaussian covariance kernel [50]) in the tangential direction. For the wall, a height of 1.5 m was chosen for the same reason, whereas full vertical dimensions were chosen for the dome and the gusset. Information concerning the geometry and the mesh of each RSV is summarized in **Table 5**.

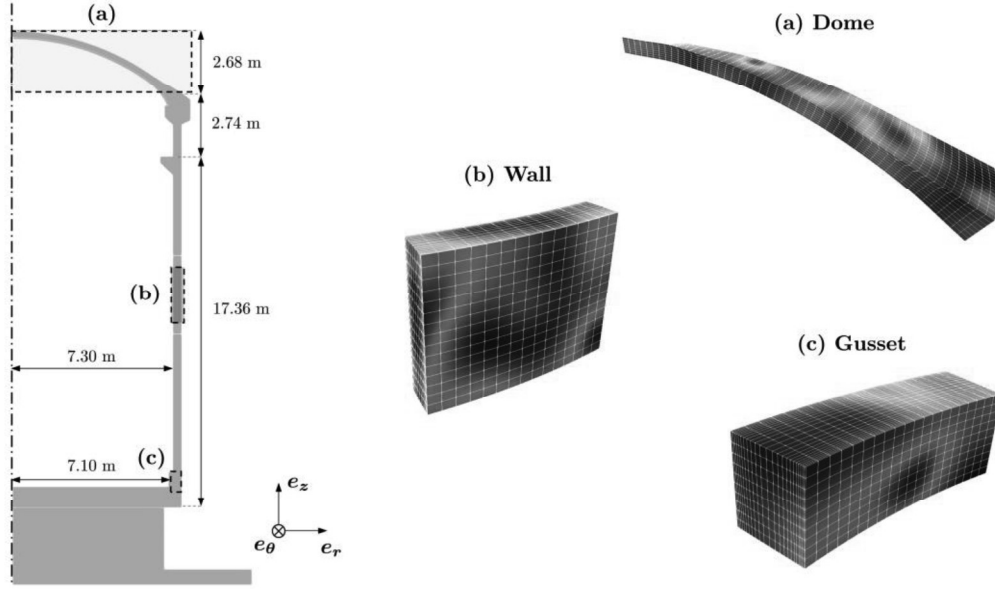


Figure 15: 2D view of the VeRCoRs mock-up (left) and some realizations of the intrinsic permeability random field on meshes of three Representative Structural Volumes (RSV) of the mock-up (right).

Table 5. Geometry and mesh of RSVs of VeRCoRs mock-up

RSV	Height [m]	Angular sector [°]	Nodes	Elements (HEXA8)
Wall	1.5		4352	3600
Gusset	0.68	15	5775	4800
Dome	2.68		7097	5910

Then, for each RSV, the log-permeability field was discretized on the corresponding FE mesh by employing the Expansion Optimal Linear Estimation (EOLE) introduced in [51]. The latter is based on a truncated version of the Karhunen-Loève (KL) expansion [49] of the log-permeability field so that the supremum norm of the error variance is below 5%. Examples of random realizations of the permeability field discretized on VeRCoRs RSVs are presented in Figure 15-a, b, and c.

517 6.2 Finite element leakage model

1
2 518 The pressurized dry air transport through a porous network is usually split into two main modes
3
4
5 519 [15,17]:

- 6
7
8 520 - diffuse porosity leakage (Darcy's mode), which refer to the leakage through concrete
9
10 521 porosity or through micro cracks
- 11
12
13 522 - localised leaks, mainly driven by the leakage through concrete macro cracks, associated
14
15 523 with Poiseuille's flow mode

16
17
18 524 This paper focuses on the Darcy's transport mode and describes a chained calculation involving
19
20 525 the computation of the thermal, hydric and hydraulic responses. Only gas transport through
21
22
23 526 sound porous concrete is considered, and the gaseous phase is assumed not to contain any
24
25 527 vapour. The dry air leakage is modelled by the following macroscopic diffusive equation:

$$\frac{d}{dt}P(x, t) = \frac{d}{dx} \left(\frac{k_a(x, t)}{2\mu} \frac{d}{dx} P^2(x, t) \right) \quad \text{Eq. 15}$$

26
27
28
29
30
31 528
32
33
34
35 529 where P is the dry air pressure, μ the air dynamic viscosity, and k_a the Darcy's apparent
36
37 530 permeability of concrete (evaluated according to saturation ratio and pressure at the location
38
39
40 531 under consideration in the wall).

41
42
43 532 The Darcy's apparent permeability term k_a is described with the following model

$$k_a(x, t) = k_i(x)\alpha_k(x, t) \quad \text{Eq. 16}$$

44
45
46
47 533 where k_i is the intrinsic permeability of concrete depending on the saturation ratio:

$$k_i(x) = k_{i0}(x)k_{rg}(x, t) \quad \text{Eq. 17}$$

48
49
50
51 534 with k_{i0} the intrinsic permeability of concrete in the dry state, k_{rg} the relative gas permeability
52
53
54 535 of concrete, and α_K a multiplicative factor accounting for the Klinkenberg effect, given by:

$$\alpha_K(x, t) = 1 + \frac{b(x, t)}{P_m} \quad \text{Eq. 18}$$

537 where $b_K(x, t)$ is the Klinkenberg coefficient, and P_m , the mean difference between the
1 538 atmospheric pressure and the pressure of the test.
2
3

4 539 Both relative gas permeability k_{rg} and the Klinkenberg coefficient b_K are assumed to be
5
6 540 dependent on the water saturation ratio of concrete, denoted by S_w . These functions are defined
7
8
9 541 only by the mean experimental curves given in Figure 7. No special variability is considered
10
11 542 for these input data as it has been verified that, compared to the spatial variability of
12
13 543 permeability obtained in field, the input data variability has a negligible impact on the final
14
15 544 prediction.
16
17

18
19 545 The water saturation ratio, S_w , is calculated through the chained thermo-hydric modelling
20
21 546 strategy presented in [52]. Concerning thermal calculations, linear Neumann boundary
22
23 547 conditions are considered on internal and external surfaces, by using in-situ measurements of
24
25 548 the temperature of the ambient air of the structure. For hydric calculations, linear relative
26
27 549 humidity (RH) fluxes are imposed on both internal and external surfaces, by using measured
28
29 550 histories of the ambient air RH. The measured histories of ambient temperature and RH are
30
31 551 given in Figure 16. During the first year after the start of construction of the mock-up, the RH
32
33 552 and the temperature of the ambient air followed seasonal conditions. Then, in order to simulate
34
35 553 an operating reactor, a heating system was started around 1.5 years after the beginning of
36
37 554 construction, in order to increase the temperature of the inner ambient air to about 35°C. The
38
39 555 temperature of the ambient air outside the mock-up inner wall was controlled, to be stabilized
40
41 556 around 20°C (see Figure 16-b). Due to the increase of the inner air temperature, the RH of the
42
43 557 inner air decreased to about 20% (see Figure 16-a) while the RH of the ambient air outside the
44
45 558 mock-up inner wall fluctuated around a value of 50%. A few weeks before each pressurization
46
47 559 test of the mock-up, the temperature of the inner air was decreased to about 15°C. This
48
49 560 temperature was maintained for a few weeks after the end of the pressurization test (see Figure
50
51 561 16-b). Due to the correlation existing between temperature and RH (typically expressed by
52
53
54
55
56
57
58
59
60
61
62
63
64
65

562 Magnus' law), this temperature decrease induced an increase of the ambient air RH, up to a
563 value of about 80%.

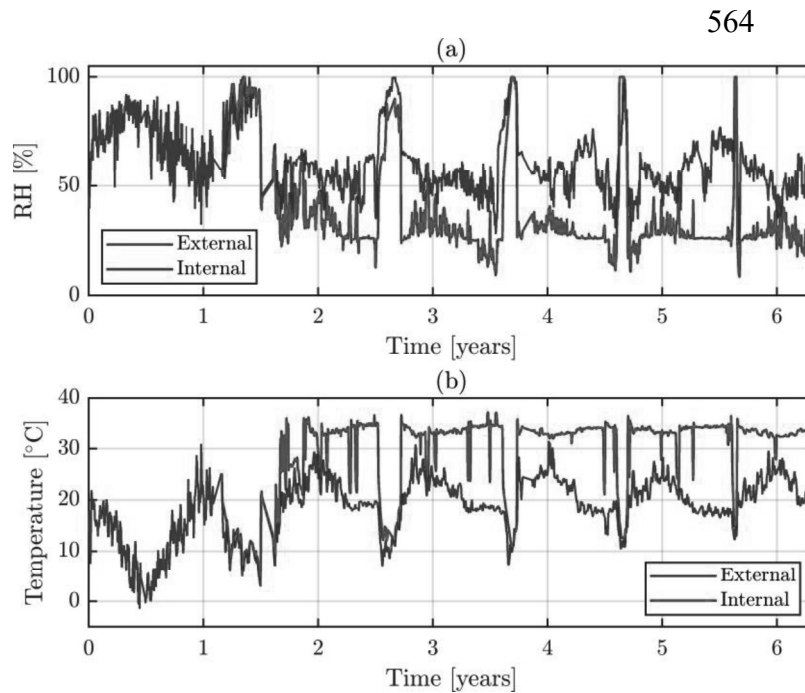


Figure 16: Measured ambient conditions of the VeRCORs mock-up : (a) RH ; (b) temperature .

573

574 Saturation profiles that were computed through a single deterministic calculation with the same
575 thermo-hydric model and boundary conditions (BC) are presented in Figure 17. Firstly, the water
576 saturation in the concrete volume decreases slightly over the 1st year. Then, due to the activation
577 of the heating system, the water saturation decreases faster, reaching a mean value of about
578 80% at t=2 years. Then, water saturation decreases to a mean value of about 65% at t=6 years
579 (about 75% in the core of the wall and lower saturation ratio close to the external surfaces). In
580 the following, the parameter B of the drying model and the initial water content $C_{w,0}$ of concrete
581 are considered as random parameters.

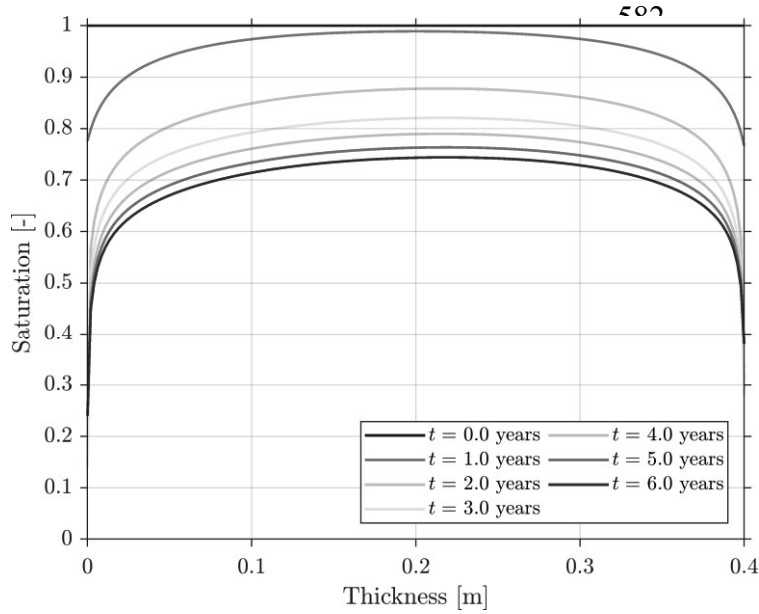


Figure 17: Water saturation profiles in the thickness of VeRCoRs' standard zone, computed through a single deterministic calculation with the adopted thermo-hydric FE model. Intrados is located at 0 m in the wall thickness.

Finally, the pressure boundaries considered were of the Dirichlet Type (overpressure on the intrados side) and the evolution was descriptive of the periodic pressurization tests. During each test, the internal air pressure was gradually increased until it reached an absolute pressure of 5.2 bars. Pressure histories associated with each test may be found in [47]. The structural Darcy's leakage rate was computed from the pressure field obtained by solving Eq. 15 and by integrating Darcy's flux on the external surface of the structure:

$$q(x, t) = \frac{-k_a(x, t)}{\eta_a} \frac{d}{dx} p(x, t) \quad \text{Eq. 19}$$

$$Q(t) = \int_{S_x \in S_{ext}} q(x, t) dS_x$$

6.3 Probabilistic diffuse leakage calculations

6.3.1. Uncertainty propagation with Polynomial Chaos Expansions (PCE)

For a given RSV, the diffuse leakage rate, Q , computed with the leakage model described in Section 6.1 may be seen as a function of d input random variables $X: \Omega \rightarrow D_X \subset R^d$, which represent the uncertain parameters of the leakage model. In this contribution, three parameters

602 are modelled by random variables in addition to the intrinsic permeability k_{i0} , which is
 603 represented by a discretized random field (see Section 6.2). These three additional parameters
 604 are given by:

- 605 • the parameter B of the drying model adopted (see [25, 29, 35]), which drives the drying
 606 speed of the concrete volume,
- 607 • the initial water content $C_{w,0}$ of concrete,
- 608 • Klinkenberg's slope $k_i \cdot b_K$.

609 This choice is justified by the fact that earlier studies have identified these parameters as those
 610 having the most influence on the diffuse leakage response at structural scale (see, e.g., [46]).

611 The characteristics of the random parameters $(B, C_{w,0}, b_K)$ and field k_0 are summarized in
 612 **Table 6**. The parameters $(B, C_{w,0}, b_K)$ are assumed to be uniform in the structure for each
 613 calculation, while the permeability, k_0 , is spatially variable, since it is modelled by a random
 614 field. We recall that the Karhunen-Loève eigenmodes of the intrinsic permeability random field
 615 are uncorrelated standard normal random variables. Furthermore, all the input parameters
 616 considered are assumed to be mutually independent.

617 **Table 6.** Characteristics of the input random parameters and the intrinsic permeability field.

Parameter	Notation	Unit	Distribution	Mean	Standard deviation	CoV
Drying parameter	B	-	Lognormal	0.08	0.016	0.2
Initial water content	$C_{w,0}$	l.m^{-3}	Lognormal	145	29	0.2
Klinkenberg's coefficient	b_K	MPa	Lognormal	0.18	0.09	0.5
Intrinsic permeability in dry state	k_0	10^{-17} m^2	Lognormal	7.0	5.25	0.75

618

1
2
3
4
5
6
7
8
9
10
11
12
13
14
15
16
17
18
19
20
21
22
23
24
25
26
27
28
29
30
31
32
33
34
35
36
37
38
39
40
41
42
43
44
45
46
47
48
49
50
51
52
53
54
55
56
57
58
59
60
61
62
63
64
65

619 Then, the quantification of the uncertainties on the leakage rate Q induced by the uncertainties
620 on the inputs is typically achieved through a Monte Carlo approach, by drawing a large sample
621 ($\sim 10^5 - 10^6$) of X and subsequently computing the corresponding output leakage rates with
622 the FE model.

623 For cost efficiency (compared to the Monte Carlo approach), surrogate modelling allows the
624 construction of a cheap approximation of the input-output map provided by the FE model, in
625 order to notably reduce the computational burden of uncertainty propagation. In this context,
626 Polynomial Chaos Expansions (PCE) [54] are widely used. The leakage response $Q(X)$
627 provided by the FE model is then approximated by a PCE, which consists of a truncated series
628 expansion formed by orthonormal polynomials [54]. Further details about the PCE surrogates
629 constructed are given in Appendix A. Then, the constructed PCE surrogate models enable a
630 global sensitivity analysis of the leakage response to be performed with respect to the input
631 random variables of the model. Sobol's sensitivity indices [55] may be computed as a by-
632 product of PCE, through analytical formulas involving PCE coefficients [56]. The time
633 evolution of the total Sobol indices of the diffuse leakage response of the structure's wall is
634 presented in Figure 18.

635 Firstly, the drying parameter B contributes most to the variance of the diffuse leakage response,
636 since its total order Sobol index is significantly larger than the Sobol indices of the other
637 parameters (Figure 18). It is also worth noting that only the first KL eigenmode ζ_1 of the intrinsic
638 permeability random field contributes significantly to the output variance. This might be
639 explained by the fact that the diffuse leakage rate is computed by integrating a Darcy flux on
640 the external surface of the structure, which induces a homogenization of fluctuations of the
641 permeability random field. For this reason, the diffuse leakage response is only sensitive to
642 large scale fluctuations of the permeability field. Moreover, the sum of all Sobol indices is

643 significantly larger than 1, notably before t=3 years, which indicates the presence of interactions
 644 between parameters.

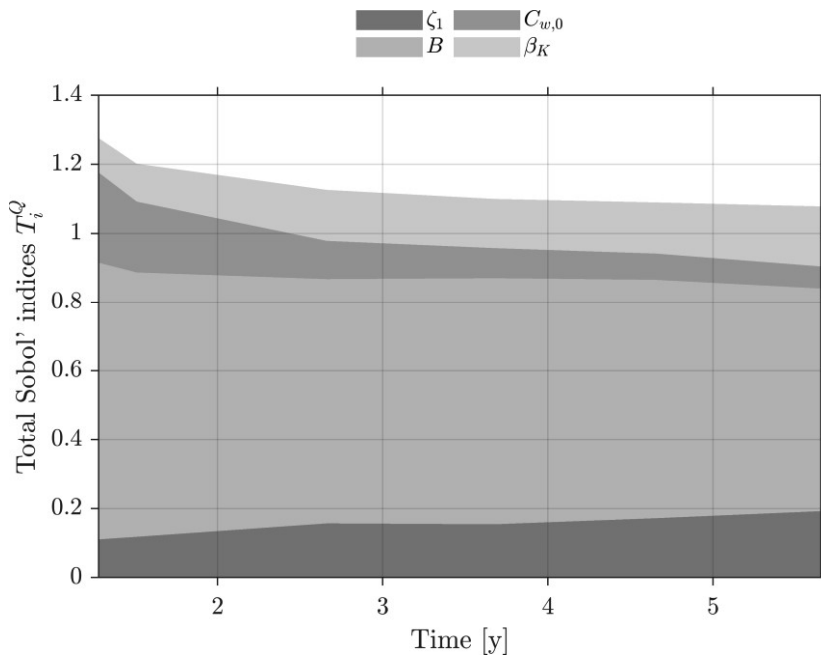


Figure 18: Time evolution of total of Sobol sensitivity indices of the diffuse leakage rate

645
 646 In order to further investigate such interactions, the most significant second order Sobol indices
 647 of the diffuse leakage response are presented in Figure 19. The drying parameter, B , presents
 648 significant interactions with the intrinsic permeability RF eigenmode ζ_1 , the initial water
 649 content $C_{w,0}$ and the Klinkenberg coefficient b_K . The contribution of these interactions
 650 decreases over time, which emphasizes the long-term behaviour of the sum of total Sobol
 651 indices, expressing a decrease in the importance of interactions.

652

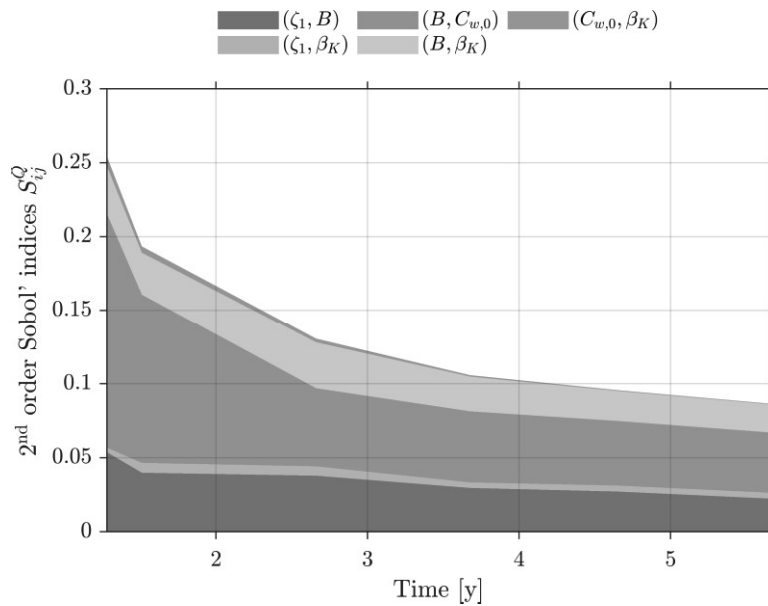


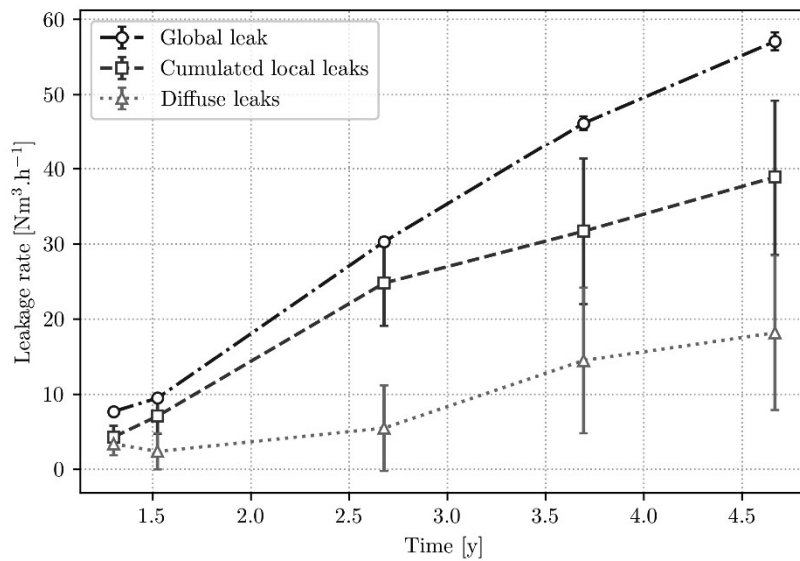
Figure 19: Time evolution of second order Sobol' indices of the diffuse leakage rate.

Finally, the global sensitivity analysis conducted underlined the very strong importance of drying parameters for the variability of the diffuse leakage response. Thus, in spite of the significant contribution of the permeability field to the variance of the leakage response, the variability of drying parameters must not be ignored when quantifying the uncertainties of the diffuse leakage response.

6.3.2. Probabilistic diffuse leakage calculations

The uncertainties of the input random parameters are propagated through the PCE surrogate model in order to compute the time evolution of the diffuse leakage rate of the VeRCoRs mock-up, together with related statistical quantities of interest such as mean and standard deviation. Before presenting a comparison of the time evolution of the predicted and measured VeRCoRs diffuse porosity leakage rates, the global leakage measurements conducted on the VeRCoRs mock-up are discussed, and presented in Figure 20. Diffuse leakage measurements are obtained in an indirect way: the global VeRCoRs leakage rate is assumed to be a superposition of two main contributions, namely Darcy leakage through concrete porosity (i.e. diffuse leaks) and leakage through cracks and possibly other types of defects (e.g. steel/concrete interfaces, casting joints) [10]. The global leakage rate is directly measured with acceptable confidence,

678 whereas the contribution of cracks is (partially) measured with leakage collecting boxes, after
 679 a visual inspection intended to locate such defects [10,57]. This measurement process presents
 680 significant uncertainties (accuracy of the measuring device according to measured air flow,
 681 quantification of the length of defects, etc.) which are transferred to the estimation of the diffuse
 682 leakage of the structure, knowing that it is computed by subtracting the total leakage of cracks
 683 from the global leakage rate. This is underlined by the fairly large error bars of the observed
 684 diffuse leakage rate shown in Figure 20. These error bars represent the 68% confidence level (i.e.
 685 the mean plus or minus one standard deviation, assuming a Gaussian distribution for
 686 measurements).



687
 688 Figure 20: Measurements of the global, local and diffuse leaks of VeRCoRs mock-up
 689 during pressurization tests. Error bars correspond to 68 % CI (i.e. mean \pm standard
 690 deviation), assuming Gaussian distributions for measurements

690

691

692

693

694

695

1

2 696

A comparison of the probabilistic predictions of the diffuse leakage rate and its measured counterpart is presented in Figure 21.

4 697

5

6

7

8

9

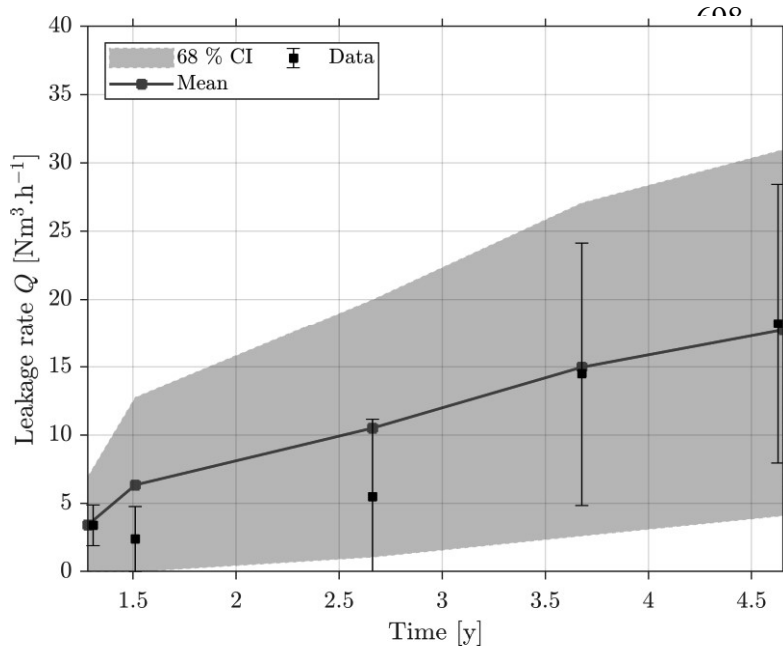


Figure 21: Probabilistic diffuse leakage predictions and comparison with measurements

707

32 708

Diffuse leakage predictions are in very good agreement with measurements, especially

33

34 709

concerning the first and the last two pressurization tests of the VeRCoRs mock-up. At the fifth

35

36 710

VeRCoRs pressurization test (~ 4.8 years), the mean predicted leakage rate ($17.7 \text{ Nm}^3 \cdot \text{h}^{-1}$)

37

38 711

approaches the mean observed diffuse leakage rate ($18.2 \text{ Nm}^3 \cdot \text{h}^{-1}$) with a relative error of about

39

40 712

3%. The modelling of the spatial variability of permeability based on surface in situ

41

42 713

measurements in vacuum (investigated depth about 70 mm) and drying parameters based on

43

44 714

previous analysis [46,53] led to a reliable predictive evaluation of the diffuse leakage rate for

45

46 715

400 mm thick concrete wall. The assumption of a mean saturation degree on the investigated

47

48 716

depth during measurements in the field is sufficient to obtain a realistic evaluation. Most of the

49

50 717

previous numerical studies performed with the leakage results obtained on the VeRCoRs mock-

51

52 718

up focused on the determination of the leakage through cracks [14,15]. Compared to the study

53

54 719

with a specific focus on the porosity leakage rate for the VeRCoRs mock-up [17], the use of in

55

56

57

58

59

60

61

62

63

64

65

720 field measurement proposed in the present work helps to obtain a more accurate prediction.

721 This work should help to accurately separate leakage from crack leakage when evaluating the
722 tightness of structures.

723 In this work, the evolution of the permeability with saturation degree was evaluated on
724 laboratory concrete samples after 60 days in limewater. Since the cement used was a CEM I,
725 the hydration should be quite stabilized after this period [20], but in real structures the hydration
726 could still have progressed after several years of atmospheric exposure. In the zones exposed
727 to dry conditions (concrete skin), the saturation level should be too low to induce additional
728 hydration for the cement. In the centre of the wall, the higher saturation conditions can lead to
729 additional hydration and thus to have lower permeability in the structure than in laboratory. But
730 the permeability used in the calculations was directly measured in field and only the
731 dependences to saturation degree and pressure can have been impacted by the differences
732 between laboratory and field. This could have led to a small misestimation of the leakage by
733 the model. An overestimation was observed for the early age of the structure (before 3.5 years)
734 and decreased with time. Combinations with other phenomena, such as the progressive drying
735 of concrete / steel interfaces, could have a greater impact than the modification of permeability
736 by cement hydration.

737 A stochastic element finite approach was used to characterize the leakage rate of the VeRCoRs
738 mock-up. The range given by the 68% credible bounds of the predicted diffuse leakage rate is
739 quite close to the experimental one. Predictions overestimate the measured leakage rates during
740 the second and third tests but values measured during these tests are nevertheless included in
741 the confidence bounds of predictions. It is also worth noting that the global measurements
742 present a sudden evolution between the third and the fourth pressurization tests. This might be
743 attributable to the quite large uncertainties on measurements, which tend to increase over time

744 (due to the fact that the number of local leaks increases and that larger local leaks are measured
1
2 745 with less accurate flowmeters), and also to several physical processes related to drying.
3
4

6 746 **7. Conclusion**

7
8 747 In this contribution, the air leakage through concrete is estimated using a novel testing technique
9
10
11 748 coupled to stochastic finite element (SFE) modelling.
12

13 749 The main results of the studies are:
14

- 15
16 750 - For the first time, both the intrinsic permeability and the slope of Klinkenberg's law
17
18 751 were evaluated from in-field measurements under vacuum using a methodology
19
20
21 752 previously proposed from a laboratory study in [12],
22
- 23 753 - 80 vacuum measurements collected on the VeRCoRs mock-up allowed the spatial
24
25
26 754 variability of intrinsic permeability to be characterized,
27
- 28 755 - The permeability data collected in the field were used to evaluate the diffuse leakage of
29
30 756 a real structure. In the case of the VeRCoRs mock-up, an SFE model of the air leakage
31
32
33 757 was built: it leads to an estimation of the mean response that is globally accurate
34
35 758 (difference of less than 10% on the flow obtained on the structure) in terms of the diffuse
36
37
38 759 air leakage under pressure),
39
- 40 760 - SFE modelling allows also the quantification of the uncertainties around the predicted
41
42
43 761 values over time.
44

45 762 In situ measurements show discrepancies in concrete permeability properties. Such variations
46
47
48 763 are associated with the intrinsic variation of the porosity of concrete coupled with drying and
49
50 764 microcracking phenomena. For the probabilistic diffuse leakage calculations, the parameters of
51
52 765 both drying and permeability equations were considered as random parameters:
53

- 54
55 766 - The contribution of the permeability field to the variance of the leakage response was
56
57 767 significant (always greater than 25%).
58
59
60
61
62
63
64
65

768 - The variability of the drying parameters (even if they are assumed to be homogeneous
 769 in structure) cannot be ignored in order to obtain a reliable quantification of the diffuse
 770 leakage uncertainties.

771 **Acknowledgements**

772 The authors acknowledge the financial support provided by MACENA and ENDE project funds
 773 (ProjetIA-11-RSNR-0009 and ProjetIA-11-RSNR-0012). The opinions presented in this paper
 774 reflect those of the authors only and do not necessarily represent the opinions of the funding
 775 agencies.

776 **Appendix A: Polynomial Chaos Expansions**

778 The input-output map given by the diffuse leakage rate Q described in Section 6.3 is
 779 approximated by a Polynomial Chaos Expansions (PCE) surrogate model, which consists of a
 780 truncated series expansion formed by orthonormal polynomials [54]:

$$781 \quad Q(X) \approx \hat{Q}(X) = \sum_{\alpha \in A} a_{\alpha} \Psi_{\alpha}(X) \quad \text{Eq. 20}$$

782 where $A \subset N^d$ is a set of multi-indices, $(a_{\alpha})_{\alpha \in A}$ the PCE coefficients, and for $\alpha = (\alpha_1, \dots, \alpha_d) \in$
 783 A Ψ_{α} is the tensorized multivariate Hermite polynomial defined by:

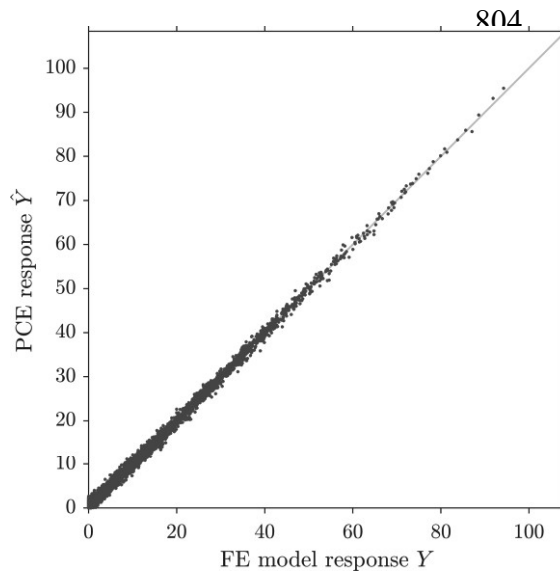
$$784 \quad \Psi_{\alpha}(X) = \prod_{i=1}^d \psi_{\alpha_i}^{(i)}(X_i) \quad \text{Eq. 21}$$

785 where $\psi_{\alpha_i}^{(i)}$ is the univariate Hermite polynomial of degree $\alpha_i \in N$.

786 In this work, the PCE coefficients $(a_{\alpha})_{\alpha \in A}$ are computed with the procedure introduced in [58],
 787 based on the Least Angle Regression algorithm (LARS). The goodness of fit between the PCE
 788 and the FE model response is quantified by computing the so-called Leave One Out (LOO)
 789 validation error (see [58,59] for further details).

790 For each pressurization test and each RSV described in Section 6.1, a PCE of the diffuse leakage
 1
 2 791 response is constructed, by considering an experimental design of size $N = 500$, generated with
 3
 4 792 the Latin Hypercube Sampling (LHS) method [60]. It is worth noting that the leakage rate of
 5
 6
 7 793 the gusset RSV may be treated as negligible, since its maximal value is smaller than 0.1
 8
 9
 10 794 $\text{Nm}^3 \cdot \text{h}^{-1}$. This may be explained by the greater thickness of the gusset (0.6 m), which induces
 11
 12 795 a larger water saturation ratio in the thickness, a smaller pressure gradient, and consequently a
 13
 14 796 lower diffuse leakage rate. Conversely, the standard zone of the structure is the main contributor
 15
 16
 17 797 to the total diffuse leakage rate (approx. 90%), especially due to its large surface area.

18
 19
 20 798 A comparison between the structural diffuse leakage rate responses computed with the FE
 21
 22 799 model and the corresponding PCE-based responses is given in Figure 20. The PCE surrogate
 23
 24
 25 800 provides a satisfactory approximation of the FE model leakage response, as underlined by the
 26
 27 801 good agreement observed between point-wise evaluations. Furthermore, the maximal LOO
 28
 29
 30 802 validation error is about 0.03 , which is an acceptable error level, compared to the threshold
 31
 32 803 values of about 0.05 usually considered in engineering practice [46,53].



811
 812 *Figure 22: Cross-plot of the PCE surrogate of the structural diffuse leakage rate response.*

814 References

- 1
2
3 815 [1] J.J. Kollek, The determination of the permeability of concrete to oxygen by the Cembureau method-a
4 816 recommendation, *Mater. Struct.* 22 (1989) 225–230. <https://doi.org/10.1007/BF02472192>.
5
6 817 [2] R.J. Torrent, A two-chamber vacuum cell for measuring the coefficient of permeability to air of the
7 818 concrete cover on site, *Mater. Struct.* 25 (1992) 358–365.
9
10 819 [3] P. Basheer, F. Montgomery, A. Long, “CLAM” tests for measuring in situ permeation properties of
11 820 concrete, *Nondestruct. Test. Eval.* 12 (1995) 53–73.
13
14 821 [4] Z. Lafhaj, G. Richard, M. Kaczmarek, F. Skoczylas, Experimental determination of intrinsic permeability
15 822 of limestone and concrete: Comparison between in situ and laboratory results, *Build. Environ.* 42 (2007)
16 823 3042–3050. <https://doi.org/10.1016/j.buildenv.2006.07.039>.
18
19 824 [5] J. Liu, F. Agostini, F. Skoczylas, From relative gas permeability to in situ saturation measurements, *Constr.*
20 825 *Build. Mater.* 40 (2013) 882–890. <https://doi.org/10.1016/j.conbuildmat.2012.11.092>.
22
23 826 [6] K. Yang, P.A.M. Basheer, Y. Bai, B.J. Magee, A.E. Long, Development of a new in situ test method to
24 827 measure the air permeability of high performance concretes, *NDT E Int.* 64 (2014) 30–40.
25 828 <https://doi.org/10.1016/j.ndteint.2014.02.005>.
27
28 829 [7] D. Zhang, K. Li, Concrete gas permeability from different methods: Correlation analysis, *Cem. Concr.*
29 830 *Compos.* 104 (2019) 103379. <https://doi.org/10.1016/j.cemconcomp.2019.103379>.
31
32 831 [8] R.J. Torrent, R.D. Neves, K.-I. Imamoto, Concrete permeability and durability performance from theory
33 832 to field applications, CRC Press, Taylor & Francis, 2022.
34
35 833 [9] E. Oukhemanou, S. Desforges, E. Buchoud, S. Michel-Ponnelle, A. Courtois, VeRCoRs Mock-Up:
36 834 Comprehensive Monitoring System for Reduced Scale Containment Model, in: *Technol. Innov. Nucl. Civ.*
37 835 *Eng. TINCE*, Paris (France), 2016.
40
41 836 [10] J.-M. Henault, P. Laviron, S. Desforges, D. Vautrin, A. Courtois, B. Martin, A. Legrix, How to characterize
42 837 the airtightness of containment structures . Overview of monitoring techniques tested on VeRCoRs Mock
43 838 up, in: *Technol. Innov. Nucl. Civ. Eng.*, Paris (France), 2018.
45
46 839 [11] R. Torrent, E. Denarié, F. Jacobs, A. Leemann, T. Teruzzi, Specification and site control of the
47 840 permeability of the cover concrete: The Swiss approach, *Mater. Corros.* 63 (2012) 1127–1133.
48 841 <https://doi.org/10.1002/maco.201206710>.
50
51 842 [12] H. Sogbossi, J. Verdier, S. Multon, New approach for the measurement of gas permeability and porosity
52 843 accessible to gas in vacuum and under pressure, *Cem. Concr. Compos.* 103 (2019) 59–70.
53 844 <https://doi.org/10.1016/j.cemconcomp.2019.04.032>.
55
56 845 [13] H. Sogbossi, Etude de l'évolution de la perméabilité du béton en fonction de son endommagement :
57 846 transposition des résultats de laboratoire à la prédiction des débits de fuite sur site, PhD thesis, Université
58 847 de Toulouse, 2017.
61
62
63
64
65

- 848 [14] T. Thénint, V. Le Corvec, S. Ghavamian, Study of the containment history of the VeRCoRS mock-up and
1 849 prediction of the leakage rate under pressurization tests, in: P.G. and C.L.B. (Eds) G. Pijaudier-Cabot
2 850 (Ed.), 10th Int. Conf. Fract. Mech. Concr. Concr. Struct. Fram., 2019.
3 851 <https://doi.org/10.21012/fc10.235607>.
4 852
5
6 852 [15] L. Charpin, J. Niepceron, M. Corbin, B. Masson, J.P. Mathieu, J. Haelewyn, F. Hamon, M. Åhs, S.
7 853 Aparicio, M. Asali, B. Capra, M. Azenha, D.E.M. Bouhjiti, K. Calonius, M. Chu, N. Herrman, X. Huang,
8 854 S. Jiménez, J. Mazars, M. Mosayan, G. Nahas, J. Stepan, T. Thenint, J.M. Torrenti, Ageing and air leakage
9 855 assessment of a nuclear reactor containment mock-up: VERCORS 2nd benchmark, Nucl. Eng. Des. 377
10 856 (2021). <https://doi.org/10.1016/j.nucengdes.2021.111136>.
11
12
13 857 [16] L. Charpin, J. Haelewyn, A.C. El Idrissi, J. Niepceron, B. Masson, C. Toulemonde, G. Boulant, J.P.
14 858 Mathieu, F. Hamon, S. Michel-Ponnell, J.M. Hénault, F. Taillade, J.L. Adia, F. Escoffier, Predicting
15 859 Leakage of the Vercors Mock-Up and Concrete Containment Buildings - a Digital Twin Approach, Acta
16 860 Polytech. CTU Proc. 33 (2022) 78–84. <https://doi.org/10.14311/APP.2022.33.0078>.
17
18
19 861 [17] T. Meng, L. Jason, T. Heitz, B. Richard, Numerical methodology on prestressed reinforced concrete
20 862 containment building: Creep, aging and leakage. Application to VERCORS mock-up, Eng. Struct. 280
21 863 (2023) 115625. <https://doi.org/10.1016/j.engstruct.2023.115625>.
22
23
24 864 [18] L. Jason, Relation endommagement perméabilité pour les bétons : application aux calculs de structures,
25 865 Nantes, 2004.
26
27
28 866 [19] V. Garnier, J.-M. Henault, H. Hafid, J. Verdier, J.F. Chaix, E. Al, Containment nuclear plant structures
29 867 evaluation by non destructive testing: strategy and results, in: TINCE 2016, 3rd Conf. Technol. Innov.
30 868 Nucl. Civ. Eng., Paris, France, 2016.
31
32
33 869 [20] V. Waller, Relations entre composition des bétons, exothermie en cours de prise et résistance en
34 870 compression, PhD Thesis, École Nationale des Ponts et Chaussées, 1999.
35
36
37 871 [21] W. Ladaoui, T. Vidal, A. Sellier, X. Bourbon, Effect of a temperature change from 20 to 50 C on the basic
38 872 creep of HPC and HPFRC, Mater. Corros. 44 (2011) 1629–1639. <https://doi.org/10.1617/s11527-011-9723-z>.
39 873
40
41 874 [22] W. Ladaoui, T. Vidal, A. Sellier, X. Bourbon, Analysis of interactions between damage and basic creep
42 875 of HPC and HPFRC heated between 20 and 80 °c, Mater. Struct. 46 (2013) 13–23.
43 876 <https://doi.org/10.1617/s11527-012-9879-1>.
44
45
46 877 [23] M. Ibro, J. Verdier, S. Geoffroy, H. Cagnon, X. Bourbon, Prediction of moisture transfer in cement-based
47 878 materials : Use of a porous network model to access transfer parameters, Cem. Concr. Res. 142 (2021)
48 879 106310. <https://doi.org/10.1016/j.cemconres.2020.106310>.
49
50
51 880 [24] A. Pichelin, M. Carcassès, F. Cassagnabère, S. Multon, G. Nahas, Sustainability, transfer and containment
52 881 properties of concrete subject to delayed ettringite formation (DEF), Cem. Concr. Compos. 113 (2020)
53 882 103738. <https://doi.org/10.1016/j.cemconcomp.2020.103738>.
54
55
56
57
58
59
60
61
62
63
64
65

- 883 [25] C. Antón, M.A. Climent, G. de Vera, I. Sánchez, C. Andrade, An improved procedure for obtaining and
1 884 maintaining well characterized partial water saturation states on concrete samples to be used for mass
2 885 transport tests, *Mater. Struct.* 46 (2012) 1389–1400.
- 3
4
5 886 [26] RILEM TC 116-PCD, Permeability of concrete as a criterion of its durability, final report, *Mater. Struct.*
6 887 32 (1999) 163–173.
- 7
8
9 888 [27] M. Carcassès, A. Abbas, J.-P. Ollivier, J. Verdier, An optimised preconditioning procedure for gas
10 889 permeability measurement, *Mater. Struct.* 35 (2001) 22–27.
- 11
12 890 [28] M.P. Yssorche, J.P. Bigas, J.P. Ollivier, Mesure de la perméabilité à l'air des bétons au moyen d'un
13 891 perméamètre à charge variable, *Mater. Struct.* 28 (1995) 401–405. <https://doi.org/10.1007/BF02473075>.
- 14
15
16 892 [29] L.J. Klinkenberg, The Permeability Of Porous Media To Liquids And Gases, in: *Drill. Prod. Pract.*,
17 893 American Petroleum Institute, 1941: pp. 200–213.
- 18
19
20 894 [30] V. Čalogović, Gas permeability measurement of porous materials (concrete) by time-variable pressure
21 895 difference method, *Cem. Concr. Res.* 25 (1995) 1054–1062.
- 22
23
24 896 [31] X. Dérobert, J. Iaquina, G. Klysz, J.P. Balayssac, Use of capacitive and GPR techniques for the non-
25 897 destructive evaluation of cover concrete, *NDT E Int.* 41 (2008) 44–52.
26 898 <https://doi.org/10.1016/j.ndteint.2007.06.004>.
- 27
28
29 899 [32] G. Villain, A. Ihamouten, X. Dérobert, Determination of concrete water content by coupling
30 900 electromagnetic methods: Coaxial/cylindrical transition line with capacitive probes, *NDT E Int.* 88 (2017)
31 901 59–70. <https://doi.org/10.1016/j.ndteint.2017.02.004>.
- 32
33
34 902 [33] S. Bonnet, J.P. Balayssac, Combination of the Wenner resistivimeter and Torrent permeameter methods
35 903 for assessing carbonation depth and saturation level of concrete, *Constr. Build. Mater.* 188 (2018) 1149–
36 904 1165. <https://doi.org/10.1016/j.conbuildmat.2018.07.151>.
- 37
38
39 905 [34] S. Multon, J. Verdier, G. Villain, H. Sogbossi, X. Derobert, H. Cagnon, J.-P. Balayssac, Non-destructive
40 906 measurements for the evaluation of the air permeability of concrete structures, *Measurement.* 196 (2022)
41 907 111204. <https://doi.org/10.1016/j.measurement.2022.111204>.
- 42
43
44 908 [35] A. Abbas, M. Carcasses, J.-P. Ollivier, Gas permeability of concrete in relation to its degree of saturation,
45 909 *Mater. Struct.* 32 (1999) 3–8.
- 46
47
48 910 [36] H. Sogbossi, J. Verdier, S. Multon, Permeability and damage of partially saturated concrete exposed to
49 911 elevated temperature, *Cem. Concr. Compos.* 109 (2020) 103563.
50 912 <https://doi.org/10.1016/j.cemconcomp.2020.103563>.
- 51
52
53 913 [37] J.F. O'Hanlon, A user's guide to vacuum technology, 3ième édit, John Wiley & Sons, 2005.
- 54
55
56 914 [38] J.G. Heid, J.J. McMahon, R.F. Nielsen, S.T. Yuster, Study of the Permeability of Rocks to Homogeneous
57 915 Fluids, in: American Petroleum Institute, 1950.
- 58
59
60 916 [39] R. Aguilera, Incorporating capillary pressure, pore throat aperture radii, height above free-water table, and

- 917 Winland r_{35} values on Pickett plots, *Am. Assoc. Pet. Geol. Bull.* 86 (2002) 605–624.
 1 918 <https://doi.org/10.1306/61EEDB5C-173E-11D7-8645000102C1865D>.
 2
 3 919 [40] F.A. Florence, J. Rushing, K.E. Newsham, T.A. Blasingame, Improved Permeability Prediction Relations
 4 920 for Low Permeability Sands, in: *Society of Petroleum Engineers*, 2007.
 5
 6
 7 921 [41] T.J. Katsube, Review of formation resistivity factor equations related to new pore-structure concepts,
 8 922 Geological Survey of Canada, 2010.
 9
 10
 11 923 [42] C. Perez-Rosales, On the Relationship Between Formation Resistivity Factor and Porosity, *Soc. Pet. Eng.*
 12 924 *J.* 22 (1982) 531–536. <https://doi.org/10.2118/10546-PA>.
 13
 14
 15 925 [43] F. Khaddour, D. Grégoire, G. Pijaudier-Cabot, Capillary bundle model for the computation of the apparent
 16 926 permeability from pore size distributions, *Eur. J. Environ. Civ. Eng.* 19 (2015) 168–183.
 17 927 <https://doi.org/10.1080/19648189.2014.939307>.
 18
 19
 20 928 [44] Y. Sakai, T. Kishi, Numerical simulation of air permeability in covercrete assuming molecular flow in
 21 929 circular tubes, *Constr. Build. Mater.* 125 (2016) 784–789.
 22 930 <https://doi.org/10.1016/j.conbuildmat.2016.08.105>.
 23
 24
 25 931 [45] Y. Sakai, Correlations between air permeability coefficients and pore structure indicators of cementitious
 26 932 materials, *Constr. Build. Mater.* 209 (2019) 541–547. <https://doi.org/10.1016/j.conbuildmat.2019.03.068>.
 27
 28
 29 933 [46] D.E.M. Bouhjiti, J. Baroth, F. Dufour, S. Michel-Ponnelle, B. Masson, Stochastic finite elements analysis
 30 934 of large concrete structures' serviceability under thermo-hydro-mechanical loads – Case of nuclear
 31 935 containment buildings, *Nucl. Eng. Des.* 370 (2020) 110800.
 32 936 <https://doi.org/10.1016/j.nucengdes.2020.110800>.
 33
 34
 35
 36 937 [47] D. Rossat, D.E.M. Bouhjiti, J. Baroth, M. Briffaut, F. Dufour, A. Monteil, B. Masson, S. Michel-Ponnelle,
 37 938 A Bayesian strategy for forecasting the leakage rate of concrete containment buildings – Application to
 38 939 nuclear containment buildings, *Nucl. Eng. Des.* 378 (2021) 111184.
 39 940 <https://doi.org/10.1016/j.nucengdes.2021.111184>.
 40
 41
 42
 43 941 [48] N. Cressie, *Statistics for Spatial Data*, John Wiley & Sons, Inc., 1993.
 44
 45 942 [49] B. Sudret, A. Der Kiureghian, *Stochastic Finite Element Methods and Reliability - A State-of-the-Art*
 46 943 *Report*, 2000.
 47
 48
 49 944 [50] E. Vanmarcke, *Random fields, analysis and synthesis*, MIT Press, Cambridge, Mass, 1983.
 50
 51 945 [51] C. Li, A. Kiureghian, Optimal Discretization of Random Fields, *J. Eng. Mech.* 119 (1993) 1136–1154.
 52
 53 946 [52] D.E.M. Bouhjiti, M. Boucher, M. Briffaut, F. Dufour, J. Baroth, B. Masson, Accounting for realistic
 54 947 Thermo-Hydro-Mechanical boundary conditions whilst modeling the ageing of concrete in nuclear
 55 948 containment buildings: Model validation and sensitivity analysis, *Eng. Struct.* 166 (2018) 314–338.
 56 949 <https://doi.org/10.1016/j.engstruct.2018.03.015>.
 57
 58
 59 950 [53] D. Rossat, J. Baroth, M. Briffaut, F. Dufour, B. Masson, A. Monteil, S. Michel-Ponnelle, Bayesian

- 951 updating for nuclear containment buildings using both mechanical and hydraulic monitoring data, Eng.
1 952 Struct. 262 (2022) 114294. <https://doi.org/https://doi.org/10.1016/j.engstruct.2022.114294>.
- 2
3 953 [54] R. Ghanem, P. Spanos, Stochastic finite elements - A spectral approach, Springer Verlag, 1991.
- 4
5 954 [55] I. Sobol, Global sensitivity indices for nonlinear mathematical models and their Monte Carlo estimates,
6 955 Math. Comput. Simul. 55 (2001) 271–280.
- 7
8
9 956 [56] B. Sudret, Global sensitivity analysis using polynomial chaos expansions, Reliab. Eng. Syst. Saf. 93 (2008)
10 957 964–979. <https://doi.org/10.1016/j.ress.2007.04.002>.
- 11
12
13 958 [57] M. Asali, Modélisation et prévision du comportement thermo-hydro-mécanique d'une paroi en béton :
14 959 application au cas des enceintes de confinement des bâtiments réacteurs nucléaires, PhD thesis, Université
15 960 Lille 1, 2016.
- 16
17
18 961 [58] G. Blatman, B. Sudret, Adaptive sparse polynomial chaos expansion based on least angle regression, J.
19 962 Comput. Phys. 230 (2011) 2345–2367. <https://doi.org/10.1016/j.jcp.2010.12.021>.
- 20
21
22 963 [59] N. Lüthen, S. Marelli, B. Sudret, Sparse Polynomial Chaos Expansions: Literature Survey and Benchmark,
23 964 SIAM/ASA, SIAM/ASA J. Uncertain. Quantif. 9 (2021) 593–649.
- 24
25
26 965 [60] M.D. McKay, R.J. Beckman, W.J. Conover, A Comparison of Three Methods for Selecting Values of
27 966 Input Variables in the Analysis of Output from a Computer Code, Technometrics. 21 (1979) 239–245.
- 28
29
30 967

Declaration of interests

The authors declare that they have no known competing financial interests or personal relationships that could have appeared to influence the work reported in this paper.

The authors declare the following financial interests/personal relationships which may be considered as potential competing interests: